CHEMISTRY
A EUROPEAN JOURNAL

C_5H_4–BR_2 Bending in Ferrocenylboranes: A Delocalized Through-Space Interaction Between Iron and Boron

Matthias Scheibitz,[a] Michael Bolte,[a] Jan W. Bats,[b] H.-Wolfram Lerner,[a] Israel Nowik,[c] Rolfe H. Herber,[c] Andreas Krapp,[d] Matthias Lein,[d] Max C. Holthausen,*[d] and Matthias Wagner*[a]

Abstract: A comparison of the molecular structures of mono-, di- and tetraborylated ferrocenes [Fc{B(R^1)(R^2)}] (R^1/R^2 = Br/Br, Br/Fc, Br/Me, Me/Me, Me/OH, OMe/OMe), 1,1′-[fc{B(R^1)(R^2)}$_2$] (R^1/R^2 = Br/Br, Br/Me, OMe/OMe), and 1,1′,3,3′-[Fe{$C_5H_3(BMe_2)_2$}$_2$] revealed the boryl substituent(s) to be bent out of the Cp ring plane towards the iron center. The corresponding dip angle α* decreases with decreasing Lewis acidity of the boron atom and with increasing degree of borylation at the ferrocene core. This trend is well reproduced by DFT calculations (including [$FcBH_2$], not yet accessible experimentally). A Bader analysis of the electron density topology of [$FcBH_2$] (α* = 26.5°; BP86/TZVP) clearly showed that there is no direct iron–boron bonding in this compound. Instead, strongly delocalized orbital interactions have been identified that involve the boron p orbital, C_{ipso} of the adjacent Cp ring, d orbitals at iron, and a through-space interaction with the second Cp ring. A second important factor is attractive electrostatic interactions, which are enhanced upon ligand bending. Cyclic voltammetric measurements on the series [$FcBMe_2$], 1,1′-[$fc(BMe_2)_2$], and 1,1′,3,3′-[Fe{$C_5H_3(BMe_2)_2$}$_2$] indicate a substantial anodic shift in the oxidation potential of the central iron atom upon introduction of BMe_2 substituents. Addition of 4-dimethylaminopyridine (DMAP) does not just counterbalance this effect, but leads to a cathodic shift of the Fe^{II}/Fe^{III} redox transition far beyond the half-wave potential of parent ferrocene. In the Mössbauer spectra, a continuous decrease in the quadrupole splitting (QS) is observed upon going from parent ferrocene to [$FcBMe_2$], to 1,1′-[$fc(BMe_2)_2$], and to 1,1′,3,3′-[Fe{$C_5H_3(BMe_2)_2$}$_2$]. In contrast, no significant differences are found between the QS values of ferrocene, [Fc(BMe_2–DMAP)], and 1,1′-[$fc(BMe_2$–$DMAP)_2$].

Keywords: boron · cyclic voltammetry · density functional calculations · metallocenes · Moessbauer spectroscopy

Introduction

Mono- ([Fc{B(R^1)(R^2)}]; Fc = (C_5H_5)Fe(C_5H_4))[1] and 1,1′-diborylated ferrocenes (1,1′-[fc{B(R^1)(R^2)}$_2$]; fc = (C_5H_4)$_2$Fe)[2] are highly interesting redox-active Lewis acids that have already found applications in various areas of research, for example, oligonuclear metallocene aggregates,[3,4] charge-transfer polymers,[5–7] difunctional chelators of Lewis bases,[8–10] ferrocene-based tris(1-pyrazolyl)borate ligands,[11–14] B–N- or B–P-bridged *ansa*-ferrocenes,[15–18] and 1,3-dibora[3]ferrocenophanes.[19] This area of research was reviewed recently.[20,21] In all these cases, the question of whether a pronounced electronic interaction between the ferrocenyl moiety and the boryl substituent(s) exists is of prime importance. Evidence has been gathered that tetracoordination of boron in [$Fc(BR_2)$] greatly facilitates iron oxidation.[5] Moreover, a crystal structure analysis of [$Fc(BBr_2)$] (two crystallographically independent molecules in the asymmetric unit) showed the BBr_2 group to be bent towards the iron atom by a dip angle α* of 17.7° (molecule I) and 18.9° (molecule II;

[a] Dipl.-Chem. M. Scheibitz, Dr. M. Bolte, Dr. H.-W. Lerner, Prof. Dr. M. Wagner
Institut für Anorganische Chemie
J.W. Goethe-Universität Frankfurt
Marie-Curie-Strasse 11, 60439 Frankfurt/Main (Germany)
Fax: (+49) 69-798-29260
E-mail: matthias.wagner@chemie.uni-frankfurt.de

[b] Dr. J. W. Bats
Institut für Organische Chemie
J.W. Goethe-Universität Frankfurt
Marie-Curie-Strasse 11, 60439 Frankfurt/Main (Germany)

[c] Dr. I. Nowik, Prof. Dr. R. H. Herber
Racah Institute of Physics
The Hebrew University of Jerusalem
91904 Jerusalem (Israel)

[d] Dipl.-Chem. A. Krapp, Dr. M. Lein, Dr. M. C. Holthausen
Fachbereich Chemie, Philipps-Universität Marburg
Hans-Meerwein-Strasse, 35043 Marburg (Germany)
Fax: (+49) 6421-28-25566
E-mail: max.holthausen@chemie.uni-marburg.de

Supporting information for this article is available on the WWW under http://www.chemeurj.org/ or from the author.

DOI: 10.1002/chem.200400690

$\alpha^* = 180° - \alpha$, whereby α is the angle between the geometric center of the carbon atoms constituting the substituted cyclopentadienyl ring, the ipso carbon atom C_{ipso}, and the boron atom).[22] These findings suggest a general opportunity 1) to monitor the coordination state of boron in ferrocenylboranes by means of the Fe^{II}/Fe^{III} redox potential and 2) to influence the Lewis acidity of the boron atom by changing the oxidation state of iron.

Here we present a detailed study on selected ferrocenylborane derivatives that differ greatly in the Lewis acidity of their boryl substituents. Special emphasis is put on answering the question of whether there is direct iron–boron interaction in ferrocenylboranes. To this end we report results from X-ray crystal structure analyses, cyclic voltammetric measurements, Mössbauer spectroscopy, and DFT calculations.

Results and Discussion

Syntheses and NMR spectroscopic characterization: All compounds investigated in the context of this paper are shown below. The prototype computational model [$FcBH_2$] (**1**) was included although it is not experimentally accessible[23] and the discussion of its structural features must be restricted to theoretical data (note that the amine adduct [Fc{$BH_2(NMe_2Et)$}] was recently synthesized and structurally characterized by X-ray crystallography[23]). Compound **1** serves as an important benchmark system, since hydrogen atoms can be expected to have only very little steric or electronic impact on the degree of iron–boron bonding. Syntheses and X-ray crystal structure analyses of [$FcBBr_2$] (**2**)[1,22] and 1,1′-[$fc(BBr_2)_2$] (**8**)[2,24] have already been published; selected structural parameters are quoted below for comparison. The mono- and diborylated ferrocenes **3**[1] and **9**[2] are accessible by methylation of **2** and **8** with neat $SnMe_4$. Sublimation (40 °C, 10^{-3} Torr) yielded single crystals of **3** and **9**. Dimethyl derivative **4** was synthesized according to a literature procedure.[1] Amber single crystals of this compound, which is normally obtained from the reaction mixture as a dark red oil, were grown by sublimation (40 °C, 10^{-3} torr). The DMAP (DMAP: 4-(dimethylamino)pyridine) adduct **4a**[5] crystallized from toluene when the solution was gradually concentrated in vacuo. Careful hydrolysis of a solution of [Fc{B(Me)Br}] (**3**) in benzene in the presence of NEt_3 led to the hydroxyboryl ferrocene [Fc{B(Me)OH}] (**5**), which bears a π-donating substituent at the boron atom that can be expected to greatly affect any electronic interaction between iron and boron. Single crystals of **5** formed serendipitously from the crude oily compound **4** upon prolonged exposure to air. Dimethoxyboryl ferrocenes **6** and **11** are readily accessible by treatment of **2** and **8** with excess $MeOSiMe_3$ in pentane and toluene, respectively. X-ray quality crystals of **6** were grown by vacuum sublimation, whereas **11** was recrystallized from hexane. The diferrocenylborane **7** can be synthesized in high yield from **2** and one equivalent of [$FcSnMe_3$][25] in benzene at ambient temperature. Crystals were obtained from a saturated toluene solution of **7**. So far, single crystals of the diborylated species **10**[2] and its DMAP derivative **10a**[5] are not available for X-ray crystallography. Nevertheless, cyclic voltammetric measurements and Mössbauer spectroscopy provided important information about the electronic structure of these compounds. The tetraborylated ferrocene **12** was synthesized from a mixture of neat 1,1′,3,3′-[Fe{$C_5H_3(BBr_2)_2$}$_2$][26] and neat $SnMe_4$ (8 equiv) at elevated temperature. Crystalline material was obtained by vacuum sublimation.

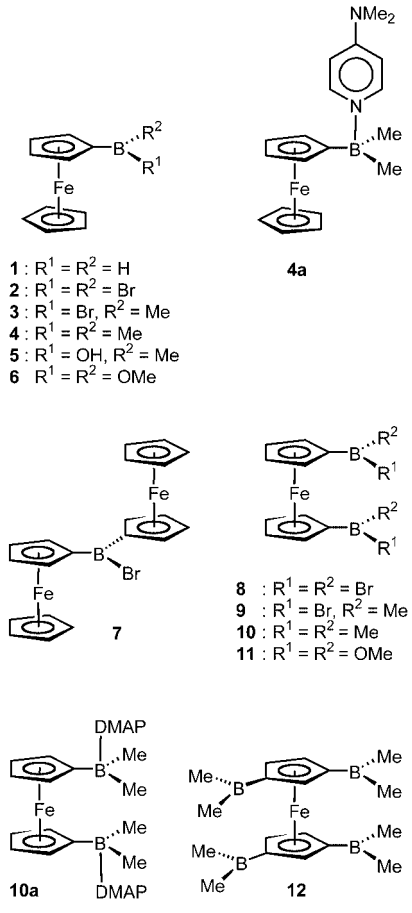

The NMR spectra of **2**,[1] **3**,[1] **4**,[1] **4a**,[5] **8**,[2] **9**,[2] **10**,[2] and **10a**[5] have been published previously. When a hydroxyl group is substituted for one of the methyl groups in **4** ($\delta(^{11}B) = 70.5$ ppm) the ^{11}B NMR resonance is shifted to higher field by 20.9 ppm (**5**: $\delta(^{11}B) = 49.6$ ppm). Replacement also of the second methyl group leads to additional magnetic shielding (**6**: $\delta(^{11}B) = 30.0$ ppm; $\Delta\delta(\mathbf{5}-\mathbf{6}) = 19.6$ ppm). There is no difference between the ^{11}B NMR shifts of **6** and **11** ($\delta(^{11}B) = 30.0$ ppm). The ^{11}B NMR resonances of diferrocenylborane **7** and tetraborylated ferrocene **12** appear at 55.3 and 74.8 ppm, respectively. The ^{1}H and ^{13}C NMR spectra of **5**, **6**, **7**, **11**, and **12** exhibit the expected signal patterns and chemical shift values and therefore do not merit further discussion (see Experimental Section).

X-ray crystal structure determinations: Selected crystallographic data of **3**, **4**, **4a**, **5**, **6**, **7**, **9**, **11**, and **12** are compiled in Table 1. In compound **3** (monoclinic, $P2_1/n$; Figure 1), the B(Me)Br substituent is disordered over two positions (occupancies: 68:32), which results in large error margins of bond lengths and angles involving the methyl carbon atom C6. Despite this deficiency, the crystal structure analysis of **3** was included in this paper, since the most important structural parameter, the dip angle $\alpha^* = 13.7°$, is not affected. Compound **4** (orthorhombic, *Pbca*; Figure 2) was chosen for a comparison of the structural characteristics of a ferrocenylborane possessing a three-coordinate boron center and its respective Lewis base adduct with a four-coordinate boryl group (**4a**; monoclinic, $P2_1/c$; Figure 3). Bromoboranes R_2BBr, such as **2** and **3**, are not suitable for this kind of investigation, because they tend to form boronium salts $[R_2B(LB)_2]^+Br^-$ upon reaction with strong Lewis bases (LB).[27] The free Lewis acid **4** exhibits a dip angle α^* of 13.0°, which is reduced to a value of $\alpha^* = 1.1°$ in the B–N adduct **4a**. At the same time, the bond between boron and

Table 1. Selected crystallographic data for **3**, **4**, **4a**, **5**, **6**, **7**, **9**, **11**, and **12**.

	3	**4**	**4a**	**5**	**6**
formula	$C_{11}H_{12}BBrFe$	$C_{12}H_{15}BFe$	$C_{19}H_{25}BFeN_2$	$C_{11}H_{13}BFeO$	$C_{12}H_{15}BFeO_2$
M_r	290.78	225.90	348.07	227.87	257.90
crystal size [mm]	0.14×0.12×0.08	0.34×0.31×0.08	0.38×0.13×0.12	0.23×0.14×0.05	0.43×0.38×0.35
crystal system	monoclinic	orthorhombic	monoclinic	triclinic	triclinic
space group	$P2_1/n$	*Pbca*	$P2_1/c$	$P\bar{1}$	$P\bar{1}$
a [Å]	10.4548(18)	9.5961(8)	9.2709(15)	11.6677(11)	10.3886(12)
b [Å]	7.6663(10)	8.7619(7)	19.940(2)	12.5059(13)	10.4644(12)
c [Å]	14.331(3)	25.580(2)	10.1081(14)	12.9675(12)	11.4338(13)
α [°]	90	90	90	97.385(8)	83.432(9)
β [°]	102.770(14)	90	113.191(11)	111.553(7)	73.997(9)
γ [°]	90	90	90	110.408(7)	76.077(9)
V [Å^3]	1120.2(3)	2150.8(3)	1717.6(4)	1576.3(3)	1158.2(2)
Z	4	8	4	6	4
ρ_{calcd} [g cm^{-3}]	1.724	1.395	1.346	1.440	1.479
T [K]	173(2)	100(2)	173(2)	100(2)	173(2)
$\mu(Mo_{K\alpha})$ [mm^{-1}]	4.867	1.355	0.878	1.395	1.281
$2\theta_{max}$ [°]	50.44	57.74	50.42	54.12	59.56
measured reflections	13666	13708	5768	23506	23192
unique reflections (R_{int})	1972 (0.103)	2800 (0.066)	2955 (0.031)	6877 (0.064)	6493 (0.086)
obsd reflections [$I>2\sigma(I)$]	1359	1876	2034	4486	5022
parameters refined	146	129	210	385	293
$R1$ [$I>2\sigma(I)$]	0.045	0.035	0.028	0.037	0.054
$wR2$ [$I>2\sigma(I)$]	0.098	0.065	0.046	0.072	0.133
GoF on F^2	0.747	0.902	0.828	0.869	0.961
largest diff. peak/hole [e Å^{-3}]	0.33/−0.45	0.29/−0.46	0.22/−0.23	0.35/−0.47	0.99/−1.23

	7	**9**	**11**	**12**
formula	$C_{20}H_{18}BBrFe_2$	$C_{12}H_{14}B_2Br_2Fe$	$C_{14}H_{20}B_2FeO_4$	$C_{18}H_{30}B_4Fe$
M_r	460.76	395.52	329.77	345.51
crystal size [mm]	0.42×0.27×0.22	0.27×0.14×0.08	0.48×0.33×0.23	0.40×0.22×0.09
crystal system	monoclinic	triclinic	monoclinic	orthorhombic
space group	$P2_1/c$	$P\bar{1}$	$P2_1/n$	$P2_12_12$
a [Å]	10.4521(8)	6.3985(12)	16.2224(9)	15.068(3)
b [Å]	12.2603(6)	6.8862(12)	9.2084(5)	7.2030(14)
c [Å]	13.8391(11)	8.4905(15)	20.2143(9)	9.1660(14)
α [°]	90	83.226(14)	90	90
β [°]	106.529(6)	81.124(14)	96.803(4)	90
γ [°]	90	67.651(13)	90	90
V [Å^3]	1700.1(2)	341.14(11)	2998.4(3)	994.8(3)
Z	4	1	8	2
ρ_{calcd} [g cm^{-3}]	1.800	1.925	1.461	1.153
T [K]	100(2)	173(2)	173(2)	155(2)
$\mu(Mo_{K\alpha})$ [mm^{-1}]	4.053	6.933	1.016	0.752
$2\theta_{max}$ [°]	55.38	50.20	51.66	63.18
measured reflections	30306	4658	56512	13193
unique reflections (R_{int})	3942 (0.052)	1217 (0.062)	5727(0.051)	3070 (0.058)
obsd reflections [$I>2\sigma(I)$]	2981	998	4764	2686
parameters refined	217	80	387	109
$R1$ [$I>2\sigma(I)$]	0.021	0.044	0.023	0.044
$wR2$ [$I>2\sigma(I)$]	0.030	0.115	0.057	0.083
GoF on F^2	0.999	1.036	0.943	1.156
largest diff. peak/hole [e Å^{-3}]	0.32/−0.41	1.20/−0.76	0.28/−0.27	0.38/−0.23

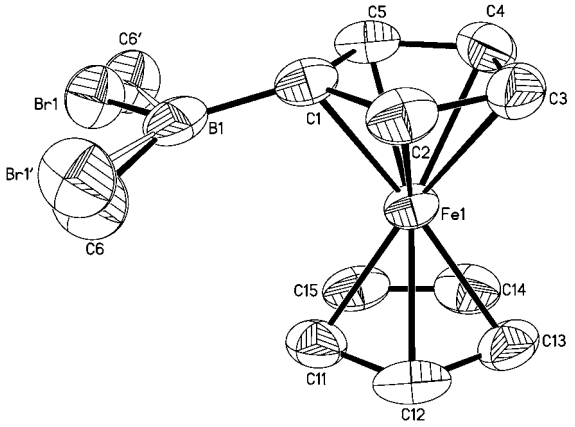

Figure 1. Molecular structure of **3**; thermal ellipsoids shown at the 50% probability level. Selected bond lengths [Å], angles [°], and torsion angles [°]: B1−C1 1.529(10), B1−C6 1.67(3), B1−Br(1) 1.868(8); C1-B1-C6 126.6(15), C1-B1-Br1 = 121.3(5), C6-B1-Br1 112.0(14); C2-C1-B1-Br1 −168.3(4), C5-C1-B1-Br1 = −8.7(8); Fe1···B1 = 2.971(8); COG-Fe1-COG* = 178.2; α^* = 13.7.

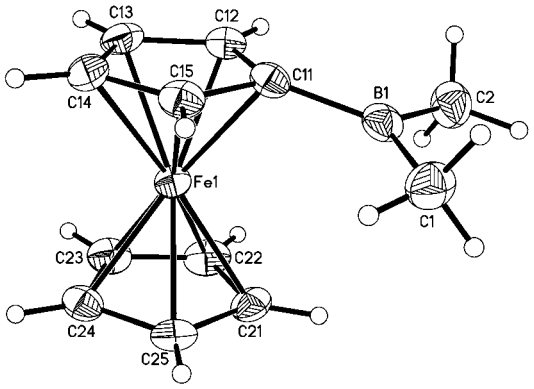

Figure 2. Molecular structure of **4**; thermal ellipsoids shown at the 50% probability level. Selected bond lengths [Å], angles [°], and torsion angles [°]: B1−C11 1.545(4), B1−C1 1.570(4), B1−C2 1.578(4); C11-B1-C1 121.1(2), C11-B1-C2 119.6(2), C1-B1-C2 119.2(2); C12-C11-B1-C1 −170.6(2), C15-C11-B1-C1 −9.5(4), C12-C11-B1-C2 11.3(4), C15-C11-B1-C2 172.4(2); Fe1···B1 3.008(3); COG-Fe1-COG* 178.2; α^* = 13.0.

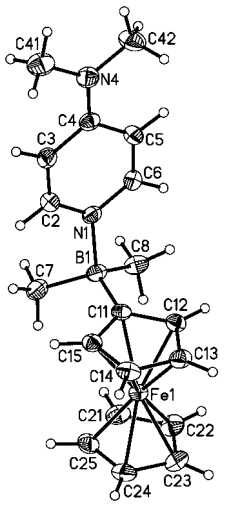

Figure 3. Molecular structure of compound **4a**; thermal ellipsoids shown at the 50% probability level. Selected bond lengths [Å], angles [°], and torsion angles [°]: B1−C11 1.625(3), B1−C7 1.622(3), B1−C8 1.619(3), B1−N1 1.670(3), C4−N4 1.352(3); C11-B1-C7 113.5(2), C11-B1-C8 112.1(2), C7-B1-C8 112.0(2), N1-B1-C11 102.7(2), N1-B1-C7 107.7(2), N1-B1-C8 108.2(2); C12-C11-B1-N1 −90.5(2), C15-C11-B1-N1 88.4(2), C11-B1-N1-C2 −85.6(2), C11-B1-N1-C6 87.4(2), C3-C4-N4-C41 −1.6(3), C5-C4-N4-C42 −0.4(3); Fe1···B1 3.347(2); COG-Fe1-COG* 178.9; α^* = 1.1.

the cyclopentadienyl ring is elongated by 0.080 Å (**4**: B1−C11 1.545(4) Å, **4a**: B1−C11 1.625(3) Å). This effect is less pronounced for the boron–methyl bonds, which are only 0.047 Å (av) longer in **4a** than in **4** (**4**: B1−C1 1.570(4) Å, B1−C2 1.578(4) Å; **4a**: B1−C7 1.622(3) Å, B1−C8 1.619(3) Å). It can therefore be concluded that the increased B1−C11 bond length in **4a** is not just caused by rehybridization of boron (**4**: sp^2 B; **4a**: sp^3 B), because this should have similar consequences for all three boron–carbon bond lengths. Even though the BMe_2 substituent is bent out of the plane of the cyclopentadienyl ring, there appears to be a considerable degree of Cp−B π bonding in **4**, which no longer exists in B−N adduct **4a**. The DMAP ligand adopts a position almost orthogonal to the substituted cyclopentadienyl ring (N1-B1-C11 102.7(2)°, C12-C11-B1-N1 −90.5(2)°). The torsion angle C11-B1-N1-C2, which characterizes the conformation of the DMAP plane relative to the $FcBMe_2$ fragment, is −85.6(2)°. As expected, a torsion angle C3-C4-N4-C41 of only −1.6(3)° is found between the NMe_2 group and the aromatic ring of the DMAP ligand; that is, N4 acts as an efficient π-electron donor towards the pyridine ring, which guarantees a high Lewis basicity of nitrogen atom N1. Despite the fact that even in solution the Lewis acid/base association/dissociation equilibrium lies quantitatively on the side of the adduct (**4a**: $\delta(^{11}B) = -3.0$), a rather long B−N bond is observed (B1−N1 1.670(3) Å). Currently, 94 adducts between sp^2 nitrogen donors and three-coordinate boron atoms are included in the Cambridge Crystal Structure File (Release 5.24 of April 2003),[28] and 84 of them have shorter B−N bonds than **4a** (cf. $(C_6F_5)_3B$−DMAP: B−N 1.602(6) Å).[29] However, this does not necessarily indicate that [$FcBMe_2$] (**4**) is a weak Lewis acid, since it is known that the correlation between the strength of a coordinative B−N bond and its length should not be overemphasized. For example, the B−N bonds in [$FcBMe_2$-pyz-Me_2BFc] (B−N 1.683(5) Å; pyz = pyrazine)[6] are not much longer than that of **4a**, despite the fact that the former compound completely dissociates in solution already at ambient temperature. Another example is the triferrocenylborane adduct [Fc_3B−pyridine], which is sterically more congested than **4a** and contains a weaker Lewis acid but nevertheless has a shorter B−N bond of 1.658(4) Å.[30]

The hydroxy derivative **5** (triclinic, $P\bar{1}$, three crystallographically independent molecules **5**, $\mathbf{5^A}$, $\mathbf{5^B}$; Figure 4) exhibits a dip angle of $\alpha^* = 10.8°$ ($\mathbf{5^A}$: 12.9°, $\mathbf{5^B}$:10.3°) and a B1−O1 bond length of 1.370(4) Å ($\mathbf{5^A}$, $\mathbf{5^B}$: 1.378(4) Å). While the dip angles in **5**, $\mathbf{5^A}$, and $\mathbf{5^B}$ are significantly larger than those found for triferrocenylboroxine ($\alpha^* = 8.0°$ (average value at 154 K)), the B−O bond lengths of both compounds lie in the same range (triferrocenylboroxine: 1.383 Å (average value at 154 K)). Molecules **5** and $\mathbf{5^B}$, which have very similar α^* values, adopt the same conformation with torsion angles H1-O1-B1-C11 of 176° and H1B-O1B-B1B-C11B of −180°. The main difference in molecule $\mathbf{5^A}$ ($\alpha^* = 12.9°$) lies in the fact that the OH group is rotated by almost 180° about the B−O bond (H1A-O1A-B1A-C11A −6°). Each molecule of **5** establishes hydrogen bonds to two neighbor-

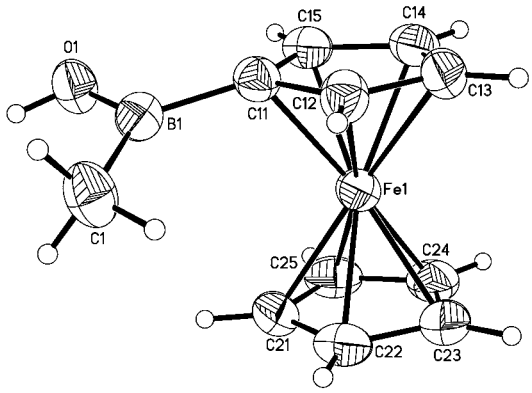

Figure 4. Molecular structure of compound **5** (**5**^{A},**5**^{B}) thermal ellipsoids shown at the 50% probability level. Selected bond lengths [Å], angles [°], and torsion angles [°]: B1−C11 1.548(4) (1.545(4), 1.547(5)), B1−C1 1.569(4) (1.576(4), 1.566(4)), B1−O1 1.370(4) (1.378(4), 1.378(4)); C11-B1-C1 123.0(3) (123.3(3), 122.9(3)), C11-B1-O1 117.9(3) (120.3(3), 117.5(3)), C1-B1-O1 119.1(3) (116.4(3), 119.6(3)); C12-C11-B1-C1 −6.0(4) (9.4(5), 8.7(4)), C15-C11-B1-C1 158.1(3) (171.0(3), 173.5(3)), C12-C11-B1-O1 174.7(3) (−170.5(3), −171.6(3)), C15-C11-B1-O1 −21.2(4) (−8.9(5), −6.7(4)), H1-O1-B1-C11 176.0 (−5.6, −179.8); Fe1···B1 3.056(3) (3.014(4), 3.057(3)); COG-Fe1-COG* 178.2 (176.9, 179.9); α^* = 10.8 (12.9,10.3); hydrogen bonds: O1−H1, O1A−H1A, O1B−H1B 0.84, H1···O1A#1 1.91, H1A···O1B#2 1.97, H1B···O1#1 1.86; O1−H1···O1A#1 175.7, O1A−H1A···O1B#2 148.4, O1B−H1B···O1#1 173.6; symmetry transformations to generate equivalent atoms: #1: $-x+2$, $-y+1$, $-z+1$; #2: $-x+2$, $-y+2$, $-z+1$.

ing molecules, whereby the hydroxyl group acts both as hydrogen-bond donor and acceptor, which may in turn have an impact on the degree of O−B π bonding and, consequently, influence the dip angle α^*.

Compared to **5**, the dip angle of dimethoxyboryl ferrocene derivative **6** (triclinic, $P\bar{1}$, two crystallographically independent molecules **6** and **6**^{A}; Figure 5) is further reduced to

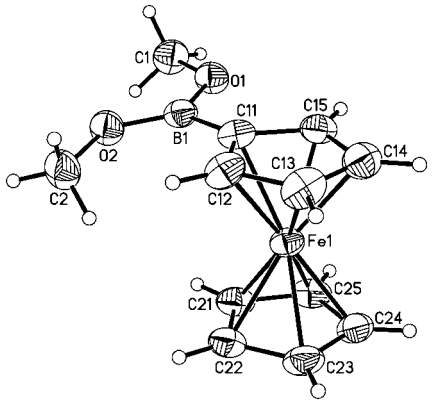

Figure 5. Molecular structure of **6** (**6**^{A}); thermal ellipsoids shown at the 50% probability level. Selected bond lengths [Å], angles [°], and torsion angles [°]: B1−C11 1.562(4) (1.556(3)), B1−O1 1.370(3) (1.368(3)), B1−O2 1.360(3) (1.360(3)); C11-B1-O1 114.9(2) (115.2(2)), C11-B1-O2 127.7(2) (127.5(2)), O1-B1-O2 117.5(2) (117.3(2)); C12-C11-B1-O1 173.6(2) (178.0(2)), C15-C11-B1-O1 −13.0(3) (−6.2(3)), C12-C11-B1-O2 −5.9(4) (−0.4(4)), C15-C11-B1-O2 167.5(2) (175.4(2)), C1-O1-B1-O2 1.5(3) (0.2(3)), C2-O2-B1-O1 178.2(2) (174.5(2)); Fe1···B1 3.179(3) (3.197(3)); COG-Fe1-COG* = 178.9 (177.9); α^* = 6.6 (5.6).

a value of 6.6° (**6**^{A}**:** 5.6°), most likely due to the presence of two π-donor substituents at boron that are, moreover, not involved in any additional hydrogen bonding. In the dinuclear species **7** (monoclinic, $P2_1/c$; Figure 6), the ferrocenyl

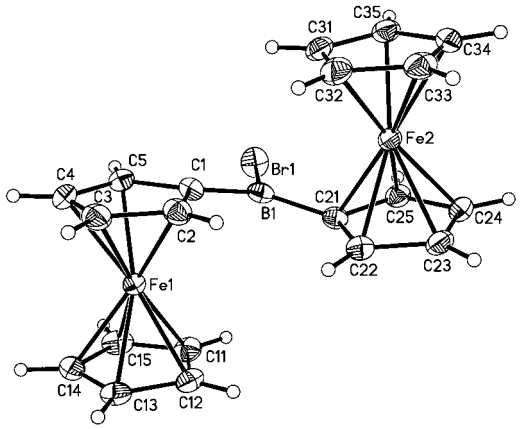

Figure 6. Molecular structure of **7**; thermal ellipsoids shown at the 50% probability level. Selected bond lengths [Å], angles [°], and torsion angles [°]: B1−C1 1.524(3), B1−C21 1.538(3), B1−Br1 1.969(2); C1-B1-C21 128.8(2), C1-B1-Br1 116.3(2), C21-B1-Br1 114.9(2); C2-C1-B1-C21 −1.5(3), C5-C1-B1-C21 −165.5(2), C2-C1-B1-Br1 179.5(2), C5-C1-B1-Br1 15.6(2), C22-C21-B1-C1 1.8(3), C25-C21-B1-C1 −156.0(2), C22-C21-B1-Br1 −179.2(2), C25-C21-B1-Br1 23.0(2); Fe1···B1 3.022(2), Fe2···B1 2.950(2); COG-Fe1-COG* 179.0, COG-Fe2-COG* 179.1; α^* 11.0 (at C1), 15.3 (at C21).

substituents adopt a *trans* arrangement with regard to the trigonal-planar boron atom (dihedral angle between C1-C2-C3-C4-C5 and C21-C22-C23-C-24-C25 9.2°). The coplanarity of the two cyclopentadienyl rings appears to be sterically less favorable than the propellerlike arrangement observed for [Fc_3B] (*cis* configuration of the three Fc substituents with regard to the trigonal-planar boron atom; dihedral angles between the borylated cyclopentadienyl rings: 39.8, 42.3, 43.7°).[31] One problem arises from the fact that the hydrogen atoms attached to C2 and C22 of **7** closely approach each other. This becomes evident from an inspection of the C1-B1-C21 angle, which is stretched to 128.8(2)°. On the other hand, steric strain is alleviated by Cp-B-Cp bending (α^* = 11.0° at C1 and 15.3° at C21; distance between H2 and H22: 2.154 Å). The molecular structure of **7** is very similar to that of the related monomeric diferrocenylborane [Fc_2BH],[23] which also shows a bent C_5H_4-B-C_5H_4 backbone with α^* values of 12.6 and 14.4° (in contrast to **7**, however, the C_5H_4-B(H)-C_5H_4 fragment is disordered about a crystallographic inversion center). Delocalization of cyclopentadienyl π electrons into the empty boron p orbital is more favorable in **7** and [Fc_2BH] than in the twisted compound [Fc_3B].

The molecular structures of the diborylated ferrocenes **9** (triclinic, $P\bar{1}$; Figure 7) and **11** (monoclinic, $P2_1/n$; Figure 8) were determined for comparison with the related monoborylated species **3** and **6**. Most relevant structural features are similar in **3**/**9** on the one hand and **6**/**11** on the other (**9**,

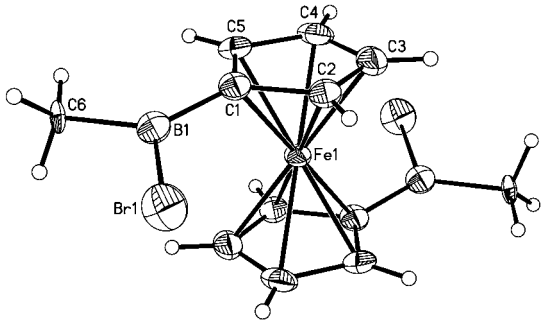

Figure 7. Molecular structure of **9**; thermal ellipsoids shown at the 50% probability level. Selected bond lengths [Å], angles [°], and torsion angles [°]: B1–C1 1.523(8), B1–C6 1.606(7), B1–Br1 1.941(6); C1-B1-C6 126.0(5), C1-B1-Br1 118.3(4), C6-B1-Br1 115.7(4); C2-C1-B1-C6 −178.4(5), C5-C1-B1-C6 −11.6(8), C2-C1-B1-Br1 1.6(7), C5-C1-B1-Br1 168.4(4); Fe1···B1 3.056(6); COG-Fe1-COG* 180.0; $\alpha^*=9.4$.

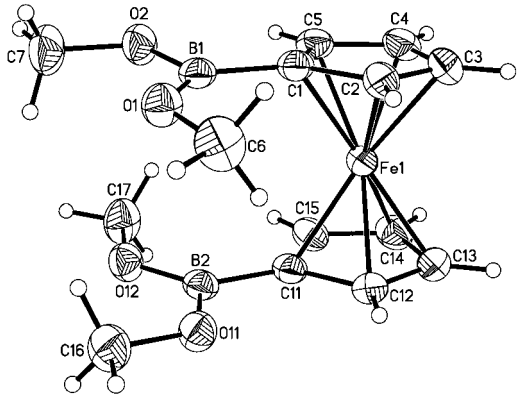

Figure 8. Molecular structure of **11** (**11**$^{\mathbf{A}}$) thermal ellipsoids shown at the 50% probability level. Selected bond lengths [Å], angles [°], and torsion angles [°]: B1–C1 1.554(2) (1.554(2)), B2–C11 1.556(2) (1.561(2)), B1–O1 1.359(2) (1.357(2)), B1–O2 1.361(2) (1.365(2)), B2–O11 1.365(2) (1.366(2)), B2–O12 1.354(2) (1.352(2)); C1-B1-O1 128.0(1) (127.7(1)), C1-B1-O2 114.6(1) (114.8(1)), O1-B1-O2 117.3(1) (117.5(1)), C11-B2-O11 115.9(1) (114.6(2)), C11-B2-O12 127.3(1) (128.4(2)), O11-B2-O12 116.8(1) (117.1(1)); C2-C1-B1-O1 −5.5(3) (−4.5(3)), C5-C1-B1-O1 172.8(1) (172.7(1)), C2-C1-B1-O2 173.1(1) (174.7(2)), C5-C1-B1-O2 −8.7(2) (−8.2(2)), C12-C11-B2-O11 −7.3(2) (−5.0(2)), C15-C11-B2-O11 174.7(1) (178.8(2)), C12-C11-B2-O12 174.2(1) (175.5(2)), C15-C11-B2-O12 −3.8(3) (−0.8(3)), C6-O1-B1-O2 179.3(2) (177.3(1)), C7-O2-B1-O1 −3.3(2) (−5.9(2)), C16-O11-B2-O12 −4.6(2) (−5.0(2)), C17-O12-B2-O11 −178.8(1) (−179.1(2)); Fe1···B1 3.226(2) (3.216(2)), Fe1···B2 3.225(2) (3.212(2)); COG-Fe1-COG* 177.6 (177.6); $\alpha^*=5.0$ (at C1), 4.2 (at C11), 6.0 (at C1A), 5.4 (at C11A).

however, does not suffer from similar B(Me)Br disorder problems as **3**), apart from the fact that introduction of a second boryl substituent into the ferrocene core leads to reduced C_5H_4–BR_2 bending (**3**/**9**: $\alpha^*=13.7/9.4°$; **6**/**11**: $\alpha^*=6.1/5.2°$ (average values)) as was already observed for **2** ($\alpha^*=18.3°$ (average value))[22] and **8** ($\alpha^*=9.1°$).[24] In contrast to **8** and **9**, which are centrosymmetric with perfectly staggered Cp ligands, both crystallographically independent molecules of **11** have their $B(OMe)_2$ substituents pointing in the same direction (**11**: C1-COG-COG*-C11 1.4°; **11**$^{\mathbf{A}}$: C1A-COG-COG*-C11A 4.6°; COG: geometric center of the Cp carbon atoms). The molecular structure of tetraborylated **12** (orthorhombic, $P2_12_12$; Figure 9) has C_2 symmetry in the crystal lattice and closely resembles the structure of 1,1′,3,3′-[Fe{$C_5H_3(BBr_2)_2$}$_2$].[26] The dip angles in **12** ($\alpha^*=6.1$, 9.3°) are considerably smaller than in monoborylated **4** ($\alpha^*=13.0°$), as was already observed in the case of **2**/**8**/1,1′,3,3′-[Fe{$C_5H_3(BBr_2)_2$}$_2$] ($\alpha^*=18.3/9.1/4.2°$ (average values)) and **6**/**11** ($\alpha^*=6.1/5.2°$ (average values)).

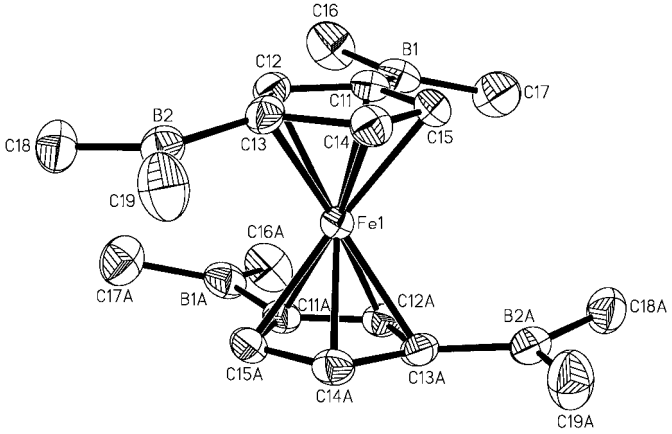

Figure 9. Molecular structure of **12**; thermal ellipsoids shown at the 50% probability level. Selected bond lengths [Å], angles [°], and torsion angles [°]: B1–C11 1.546(3), B2–C13 1.548(3), B1–C16 1.566(4), B1–C17 1.573(4), B2–C18 1.571(3), B2–C19 1.571(4); C11-B1-C16 120.2(2), C11-B1-C17 120.7(2), C16-B1-C17 119.1(2), C13-B2-C18 121.1(2), C13-B2-C19 119.9(2), C18-B2-C19 119.0(2); C12-C11-B1-C16 15.3(3), C15-C11-B1-C16 −173.8(2), C12-C11-B1-C17 −166.4(2), C15-C11-B1-C17 4.5(3), C12-C13-B2-C18 −3.1(3), C14-C13-B2-C18 −170.0(2), C12-C13-B2-C19 176.3(2), C14-C13-B2-C19 9.5(3); Fe1···B1 3.164(3), Fe1···B2 3.096(3); COG-Fe1-COG* 177.3; $\alpha^*=6.1$ (at C11), 9.3 (at C13); symmetry transformations to generate equivalent atoms: A: $-x+1$, $-y+1$, z.

The conformation adopted by the $B(R^1)(R^2)$ substituent(s) in **2**–**9**, **11**, and **12** with respect to the ferrocenyl fragment brings the formally empty boron-centered p orbital(s) into a position parallel to the filled p orbital(s) of the ipso carbon atom(s). However, any Cp–B π interaction is likely to be disfavored by bending of the boryl substituent out of the plane of the cyclopentadienyl ring towards the iron atom, as is observed for **2**–**9**, **11**, and **12**. The question thus arises whether this structural feature is caused by a direct iron–boron interaction, which could also lead to transfer of electron density into the boron p orbital and thus outweigh the decreased Cp–B π bonding. As far as the monoboryl ferrocenes are concerned, a gradual decrease of α^* values is observed (Figure 10) upon going from **2** ($\alpha^*=18.3°$ (average value)) to **3** ($\alpha^*=13.7°$), **4** ($\alpha^*=13.0°$), **5** ($\alpha^*=11.3°$ (average value)), and **6** ($\alpha^*=6.1°$ (average value)). The Fe···B distances are found to increase in the same order (**2**: 2.840/2.856 Å, **3**: 2.971(8) Å, **4**: 3.008(3) Å, **5**: 3.014(4)/3.056(3)/3.057(3) Å, **6**: 3.179(3)/3.197(3) Å). In the diferrocenyl borane **7**, α^* values of 15.3 and 11.0° correspond to Fe···B bond lengths of 2.950(2) Å and 3.022(2) Å, respectively.

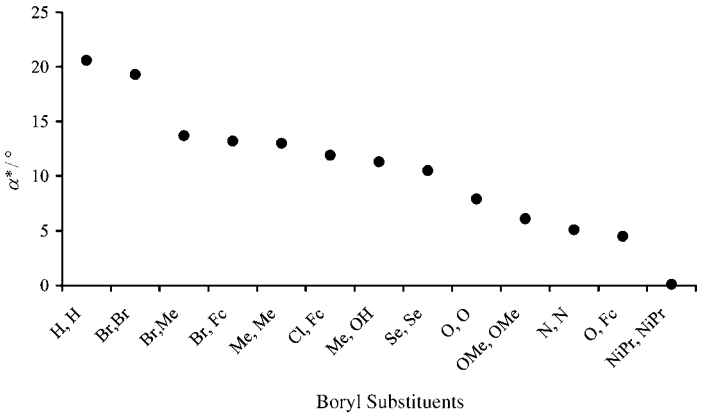

Figure 10. Correlation between dip angle α^* and the boryl substituents of selected derivatives [FcB(R^1)(R^2)].

Here, two FcB fragments of identical chemical composition differ in dip angle by as much as 4.3°, which indicates a rather shallow potential-energy surface related to the Cp–B(R^1)(R^2) bending mode. This conclusion is further supported by the significantly different α^* values of the three crystallographically independent molecules of **5** ($\Delta\alpha^* = 2.6°$). Smaller dip angles than in the monoborylated compounds **2**–**7** are found in the corresponding 1,1′-diborylated species **8** ($\alpha^* = 9.1°$), **9** ($\alpha^* = 9.4°$), and **11** (**11**: $\alpha^* = 4.2°$, 5.0°; **11**$^{\mathbf{A}}$: 5.4°, 6.0°). Compound **2**, which has the largest dip angle α^*, shows the shortest B–Cp bond (17.7°/1.482(8) Å and 18.9°/1.474(9) Å for the two crystallographically independent molecules), while **4**, which has a smaller dip angle ($\alpha^* = 13.0°$), shows a much longer B–Cp bond (B1–C11 1.545(4) Å). This correlation, which can be seen in most other ferrocenylborane derivatives, is inverse to the trend expected for the simple picture of competing Fe–B σ and Cp=B π interactions. We investigate the electronic basis of these observations by quantum chemical means below.

To get a more complete overview, two other series of closely related ferrocenylborane derivatives must be considered: 1) Crystal structure analyses of triferrocenyltriselenatriborinane [$(FcBSe)_3$],[32] triferrocenylboroxine [$(FcBO)_3$],[33] and triferrocenylborazine [$(FcBNH)_3$][33], all of which have a central six-membered ring with pendant ferrocenyl substituents at the boron atoms, revealed dip angles α^* of 10.5, 7.9, and 5.1°, respectively. 2) Apart from **7** ($\alpha^* =$ 13.2° (average value)) and [Fc_2BH] ($\alpha^* = 13.5°$ (average value)), two other diferrocenylboranes have been structurally characterized. These are the chloro compound [ClB($fcSiMe_2Cl$)$_2$] ($\alpha^* = 11.9°$ (average value), in which the borylated cyclopentadienyl rings and the BCl bridge are disordered over two positions with occupancies of 50:50),[34] and the oxo-bridged tetraferrocene aggregate [$(ClMe_2Sifc)_2$-BOB($fcSiMe_2Cl$)$_2$] ($\alpha^* = 4.5°$ (average value)).[34] In both series, the dip angles decrease as the degree of B–X π bonding increases (X = Se, O, N; Br, Cl, O). The smallest dip angles of all three-coordinate ferrocenylboranes investigated so far were found for 1,1′-[fc{B(N*i*Pr$_2$)$_2$}$_2$], which bears two strongly π-donating diisopropylamino groups at each of its boryl substituents ($\alpha^* = -1.8°$, 2.8°).[24] In this special case, however, the steric bulk of the N*i*Pr$_2$ groups might have a strong influence on the size of α^* as well.

The data collected in this section clearly reveal a causal relationship between the Lewis acidity of the boryl group in ferrocenylboranes and the dip angle α^*: The more Lewis acidic the B(R^1)(R^2) substituent is, the more it is bent towards the iron atom. This effect is less pronounced in 1,1′-diborylated and 1,1′,3,3′-tetraborylated ferrocenes than in the monoborylated species.

Electrochemical measurements: All potentials are referenced against the FcH/FcH^+ redox couple; where necessary, literature data used for comparison were recalculated for FcH/FcH^+ as reference. The cyclic voltammograms of **4**, **10**, and **12** (CH_2Cl_2, 0.1 M NBu_4PF_6) exhibit redox transitions with half-wave potentials $E^{\circ\prime}$ of +0.09, +0.26, and +0.39 V, respectively. When the scan rates are varied from 0.02 to 1.00 V s^{-1}, the current ratio i_{pc}/i_{pa} is constantly equal to 1, the current function $i_{pa}/v^{1/2}$ remains constant, and the peak-to-peak separation does not depart appreciably from the value of 59 mV theoretically expected for an electrochemically reversible one-electron process. Thus, any possible structural reorganizations accompanying iron oxidation in **4**, **10**, and **12** must be fast and reversible. Introduction of BMe_2 substituents into the ferrocene core increases the oxidation potential of the central iron atom. This anodic shift, which is apparently additive, can be attributed to the π-electron-withdrawing nature of three-coordinate boryl groups. Addition of DMAP (1 equiv for **4**, 2 equiv for **10**) with subsequent B–N adduct formation does not just neutralize this effect, but leads to a cathodic shift of the Fe^{II}/Fe^{III} redox transition far beyond the half-wave potential of parent ferrocene [$E^{\circ\prime}$(**4a**) = −0.40 V (CH_2Cl_2), $E^{\circ\prime}$(**10a**) = −0.66 V (CH_2Cl_2)].[5]

^{57}Fe Mössbauer spectroscopy (MS): As is true for all neutral ferrocene-related compounds, the Mössbauer spectra of **4**, **4a**, **10**, **10a**, and **12** consist of simple well-resolved doublets that can be characterized in terms of their isomeric shift (IS), quadrupole splitting (QS), and area under the resonance curve (A). As a typical example the spectrum of **4** at 90 K is shown in Figure 11; MS parameters of all compounds investigated are summarized in Table 2.

*Compounds **4** and **4a***: Similar to all other derivatives examined in this study, the IS of **4** (0.524 ± 0.004 mm s^{-1} at 90 K) is very similar to that of parent ferrocene (0.537 ± 0.001 mm s^{-1} at 90 K). In consonance with previous observations,[35–37] ring substitution of a B(CH_3)$_2$ group for a hydrogen atom has only a small effect on the s electron density at the metal center. The effective vibrating mass[38] of the metal atom M_{eff}, calculated from the temperature dependence of the IS, is 107 Dalton. The difference between this value and the "bare" iron atom mass of 57 Dalton is a measure of the covalency of the iron–ligand interaction in these

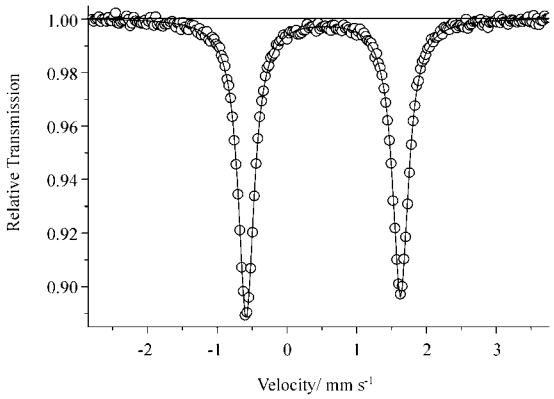

Figure 11. ^{57}Fe Mössbauer spectrum of **4** at 90 K. The velocity scale is with respect to the centroid of a room-temperature α-Fe spectrum.

Somewhat counterintuitively, the QS parameter observed for **4a** (2.344 ± 0.003 mm s^{-1}) is rather similar to the value measured for **4**, even though a pronounced difference of 0.49 V is observed in the redox potentials of the two compounds (**4**: $E^{\circ\prime} = +0.09$ V, **4a**: $E^{\circ\prime} = -0.40$ V). In the case of solid **4a**, MS spectra were acquired up to 340 K. Such measurements were not possible for free **4** due to its lower melting point. The high-temperature spectra of **4a** revealed a marked deviation from linearity in the $\ln f$ plot, especially for temperatures above 250 K, as is also observed in the corresponding data for **4** (cf. discussion for **10**/**10a** below). This nonlinearity presumably arises from the onset (upon warming) of additional vibrational modes of the iron atom, associated with the onset of ring rotation in the monoborylated species.

Table 2. Mössbauer parameters for **4**, **4a**, **10**, **10a**, and **12.** Values in parentheses are estimated errors in the last significant figure(s).

	4	**4a**	**10**	**10a**	**12**
IS(90) [mm s^{-1}]	0.524(4)	0.515(3)	0.528(4)	0.520(4)	0.546(4)
QS(90) [mm s^{-1}]	2.309(4)	2.344(3)	2.082(4)	2.339(4)	1.891(4)
$-$d(IS)/dT [mm s^{-1} K^{-1} $\times 10^{-4}$]	3.91(15)	4.75(37)	3.17(41)	3.17(6)	4.02(11)
$-$d(ln$A$)/dT [K^{-1} $\times 10^{-3}$]	9.57(5)	5.42(14)	12.9(3)	11.1(1)	7.94(17)
M_{eff} [Dalton]	107(10)	130(12)	131(13)	131(13)	104(1)
θ_{M} [K]	87	105	68	73	97
vibrational anisotropy	small	small	above ca. 180 K	small	moderate

*Compounds **10** and **10a***: The MS parameters of **10** and **10a** are summarized in Table 2. The M_{eff} of iron is about 22% larger in **10** than the M_{eff} calculated for monoborylated **4**. However, θ_{M} is 23% lower in **10** relative to **4**, consistent with the observation that **10** is a liquid at room temperature, while **4** is a semisolid. The QS parameter is significantly smaller for **10** relative to **4**, presumably due to the presence of two rather than one electron-withdrawing boryl substituents. The vibrational anisotropy observed for the iron atom in **10** is illustrated in Figure 13. Especially at higher temperatures, the Mössbauer spectra show a temperature-dependent intensity ratio R, which is related to the change in the motional anisotropy $[k^2\langle x_{\parallel}^2\rangle - k^2\langle x_{\perp}^2\rangle]$ of the iron atom.[42] On the other hand, the recoil-free fraction f is

ferrocenoids. The temperature dependence of ln$A$, which can be related to the mean-square amplitude of vibration $\langle x^2\rangle$ of the iron atom, is a linear function over the temperature range of 86–273 K. From the temperature dependence of the IS and ln$A$ we calculate a Mössbauer lattice temperature[38] θ_{M} of 87 K. The iron atom in **4** exhibits only a small vibrational anisotropy in the crystalline phase, in consonance with the ORTEP representation in Figure 2. The QS of **4** (2.309 ± 0.004 mm s^{-1} at 90 K) is significantly smaller than that of ferrocene (2.418 mm s^{-1} at 90 K). The relationship between the QS of ferrocene derivatives and the electron-withdrawing properties of the ring substituents has been discussed in detail previously.[39–41] We note an interesting observation connected to the QS parameter. When the sample, which had originally been cooled rapidly from room temperature to 78 K, is examined in a warming mode, the QS has a value of about 2.21 mm s^{-1} and is essentially temperature-independent up to 200 K. Above this temperature, the QS rapidly rises to 2.27–2.31 mm s^{-1} and remains at this higher value even if the sample is subsequently cooled back to 90 K. This sequence is summarized graphically in Figure 12. When this sample is warmed to about 310 K for periods of up to 60 min, cooled, and then re-examined, a higher QS value of about 2.31 mm s^{-1} is observed, essentially independent of temperature. To explain these findings we note that for glove-box transfer (vide infra) the sample had been warmed above its melting point. Upon rapid cooling it first sets to a supercooled liquid at 78 K, which is then annealed to the crystalline state upon slow warming to 210 K.

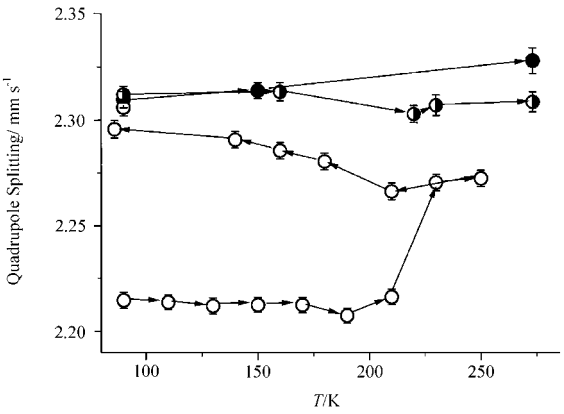

Figure 12. Temperature dependence of the QS parameter of **4**. The original sample was rapidly quenched from room temperature to 78 K. Data for the initial warming regime are indicated by open circles and the sequence by arrows. A second warming data set is represented by the filled and half-filled circles. These data are considered identical within experimental error. The low QS values are ascribed to a supercooled liquid phase which converts to the stable crystallographic phase at about 200 K (see text).

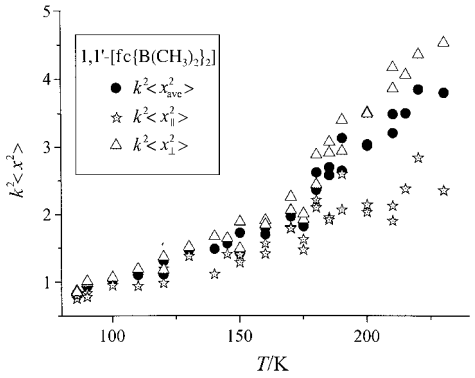

Figure 13. The $k^2\langle x^2\rangle$ parameter as a function of temperature for **10**, as discussed in the text. The filled circles are the average values determined from the recoil-free fraction data. The triangles reflect the motion perpendicular to the local symmetry axis, and the stars that parallel to this axis.

related to the average square of the motional amplitude by the relation $f=\exp(-k^2\langle x^2\rangle)$, in which k is the wave vector of the 14.4 keV radiation. Thus, from R and f it is possible to calculate mean-square amplitude of vibration parallel and perpendicular to the molecular symmetry axis, assuming that $k^2\langle x^2_{av}\rangle = 1/3\,k^2\langle x^2_{\|}\rangle + 2/3\,k^2\langle x^2_{\perp}\rangle$ (cf. Figure 13). Below 170 K the difference between $[\langle x^2_{\perp}\rangle]^{1/2}$ and $[\langle x^2_{\|}\rangle]^{1/2}$ is small, but it becomes appreciable at higher temperatures (e.g., 0.12 Å at 190 K, and 0.16 Å at 210 K). Moreover, as illustrated in Figure 13, this anisotropy is a reflection of the larger $[\langle x^2_{\perp}\rangle]^{1/2}$ term relative to $[\langle x^2_{\|}\rangle]^{1/2}$ at higher temperatures. In contrast to the **4**/**4a** couple with rather similar QS values, **10a** has a QS value 0.257 mm s^{-1} larger than that of the free Lewis acid **10**. As was true for **10** and **4**, the vibrational anisotropy of the iron atom is somewhat larger in **10a** than in **4a**. As for **4** it was not possible to obtain Mössbauer spectra at temperatures above 230 K due to the liquid nature of **10** at room temperature.

*Compound **12***: Because this compound melts to a red liquid just above room temperature, MS data were acquired only in the range $86 < T < 273$ K (Table 2), yet adequate temperature-dependent parameters could readily be extracted from these measurements. The IS(T) plot is well fitted by a linear regression (slope $= -(4.02 \pm 0.11) \times 10^{-4}$ mm s^{-1} K^{-1}) with a correlation coefficient of 0.997 for 13 data points. The corresponding M_{eff} is 104 ± 1 Dalton. Likewise, the temperature dependence of the recoil-free fraction is linear over the whole temperature range. From these two slopes an effective lattice temperature as "seen" by the iron atom of $\theta_M =$ 97 K can be extracted. Moreover, data acquired in a warming/cooling cycle (between 90 and 273 K) show the MS hyperfine parameters to be completely reversible. A moderate vibrational anisotropy is evident in the MS data; however, because of the limitations in the accessible temperature range we refrain from translating this into a quantitative measure[43] of the vibrational amplitudes parallel and perpendicular to the major symmetry axis passing through the metal atom. The magnitude of the QS parameter of **12** (1.891 ± 0.004 mm s^{-1} at 90 K) is the smallest observed for the dimethylboryl complexes examined in this study. An investigation of the hypothetical DMAP tetraadduct **12a** would be desirable. Unfortunately we found this compound experimentally inaccessible, because the ferrocene backbone of **12** decomposed upon addition of 4 equiv of DMAP, as indicated by NMR spectroscopy.

Quantum chemical calculations: We commence the theoretical part of the present study by a calibration of quantum chemical methods for the description of molecular geometries and donor–acceptor binding energies for the present class of compounds. The results of these systematic benchmarks and a detailed discussion are provided as Supporting Information. In summary, notwithstanding some problems in the description of B–N bond strengths, which strike all functionals tested more or less equally and for which no cure is evident at present, we found that the BP86/TZVP level in combination with the Ahlrichs TZVP-J Coulomb fit basis is a computationally efficient level of theory that performs very well in predicting the structures of borylated ferrocenes. All results reported below were obtained at this level of density functional theory by using its highly efficient implementation in the TURBOMOLE program. The theoretical strategies employed in the present study are detailed below (see Experimental Section and Computational Methods). Figure 14 illustrates key geometric parameters discussed in the following.

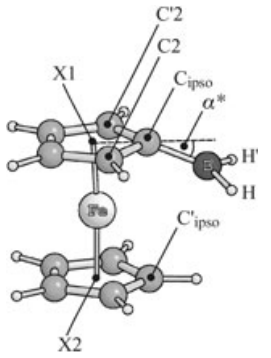

Figure 14. Illustration of geometric parameters discussed in the text, given for the example of **1** and referred to in the Supporting Information.

Computed redox potentials—correlation with cyclic voltammetric and ^{57}Fe Mössbauer data: As a qualitative approximation to assess the results from the cyclic voltammetric experiments by quantum chemical means, we computed the adiabatic ionization potentials at the BP86/TZVP/RI(TZVP-J) level employing the COSMO continuum model (solvent dichloromethane, dielectric constant at room temperature $\varepsilon = 8.93$). For parent ferrocene we compute an adiabatic ionization energy (IE) of 5.14 eV, which is used as reference in the following discussion. Introduction of BMe_2 substituents into the ferrocene core leads to an increase in the corresponding computed ΔIE (data relative to FcH = 0.00 eV: **4** 0.15 eV, **10** 0.24 eV, **12** 0.39 eV; see Table 3). We assign this effect, which is also reproducible with other substituents BRR′ (R, R′ = Me, F, Cl, Br, I, OH; see Table 3), to the π-electron-withdrawing nature of the three-coordinate boron atom. The only exception is $FcB(NH_2)_2$, for which we find an IE of -0.09 eV relative to FcH. Here, the electron deficiency of the boron atom is evi-

Table 3. Adiabatic ionization energies (IE) computed from total energy differences obtained at the BP86/TZVP/RI(TZVP-J)+COSMO(CH_2Cl_2, $\varepsilon=8.93$) level of density functional theory for substituted ferrocenes FcR. All calculations were performed without molecular symmetry (C_1). Experimental redox potentials (see text): **4**: 0.09 V, **4a**: −0.40 V, **10**: 0.26 V, **10a**: −0.66 V, **12**: 0.39 V (in CH_2Cl_2 vs FcH/FcH^+).

Species	IE [eV]	ΔIE (Fc/Fc^+) [eV]	α^* (neutral/ion) [°]
[FcH]	5.14	0.00	
[$FcBH_2$] (**1**)	5.48	0.34	25.1/5.0
[$FcBMe_2$] (**4**)	5.29	0.15	13.2/3.6
[FcB(Me)Br] (**3**)	5.42	0.28	12.1/3.3
[FcB(Me)(OH)] (**5**)	5.19	0.05	6.1/2.2
[$FcBF_2$]	5.45	0.31	10.5/2.8
[$FcBCl_2$]	5.52	0.38	11.9/3.0
[$FcBBr_2$] (**2**)	5.54	0.40	13.2/3.6
[$FcBI_2$]	5.52	0.38	14.4/1.1
1,1′-[fc(BMe_2)$_2$] (**10**)	5.38	0.24	10.7, 10.2/2.3, 2.1
1,1′,3,3′-[fc(BMe_2)$_4$] (**12**)	5.53	0.39	$(6.3, 3.9)_U$ $(6.1, 3.5)_L$/ $(1.4, 0.8)_U$ $(1.2, 0.9)_L$[a]
[$FcB(NH_2)_2$]	5.05	−0.09	1.5/0.7
[Fc(BH_2–pyridine)]	4.83	−0.31	0.1/2.7
[Fc(BMe_2–DMAP)] (**4a**)[b]	4.71	−0.43	−3.2/0.0
1,1′-[fc(BMe_2–DMAP)$_2$] (**10a**)	4.54	−0.60	−2.2, −2.3/−0.4, −0.6

[a] α^* values grouped in parentheses refer to upper and lower Cp rings, respectively. [b] Data for the perpendicular conformer (see text). ΔIE for the collinear conformer is −0.38 eV.

dently already fully compensated by the two π-electron-donating NH_2 groups. This interpretation is in line with the fact that we find in neutral [$FcB(NH_2)_2$] only a minute dip angle $\alpha^*=1.5°$ and an almost planar $B(NH_2)_2$ moiety, which is tilted by 24° out of the plane of the adjacent Cp ring. Hence, it appears that the above-mentioned corresponding properties of the 1,1′-[fc{B(N*i*Pr$_2$)$_2$}$_2$] derivative are not only caused by steric bulk, but rather are a consequence of efficient N→B π donation. The higher IE of **4** agrees nicely with the experimental observation of an anodic shift of its redox potential ($E^{0\prime}=+0.09$ V) relative to the FcH reference. As stated above the QS of ferrocenes in Mössbauer spectroscopy becomes smaller upon substitution by electron-withdrawing groups. The QS value of **4** (−0.109 mm s^{-1} at 90 K vs FcH) thus correlates both with the calculated ΔIE and the anodically shifted redox potential. Considering also the di- and tetraborylated derivatives, common trends become apparent 1) for redox potentials, which are shifted to more positive values along the series FcH ($E^{0\prime}=0.00$ V), **4** ($E^{0\prime}=+0.09$ V), **10** ($E^{0\prime}=+0.26$ V), and **12** ($E^{0\prime}=+0.39$ V), and 2) for the quadrupole splittings, which show a corresponding decrease (Figure 15) from FcH (QS = 2.418 mm s^{-1}) to **4** (QS = 2.309 mm s^{-1}), **10** (QS = 2.082 mm s^{-1}), and **12** (QS = 1.891 mm s^{-1}). Adduct formation of **4** and **10** with DMAP leads to a cathodic shift of the redox potentials of **4a** ($E^{0\prime}=-0.40$ V vs FcH/FcH^+ or $E^{0\prime}=-0.49$ V vs **4**/**4**$^+$) and **10a** ($E^{0\prime}=-0.66$ V vs FcH/FcH^+ or $E^{0\prime}=-0.92$ V vs **10**/**10**$^+$). This trend is well reproduced by the calculated ΔIEs (**4a**: −0.43 eV vs FcH/FcH^+ or −0.58 eV vs **4**/**4**$^+$; **10a**: −0.60 vs FcH/FcH^+ or −0.84 eV vs **10**/**10**$^+$). Even though it has experimentally been established that electron-donating substituents at FcH cause an increase

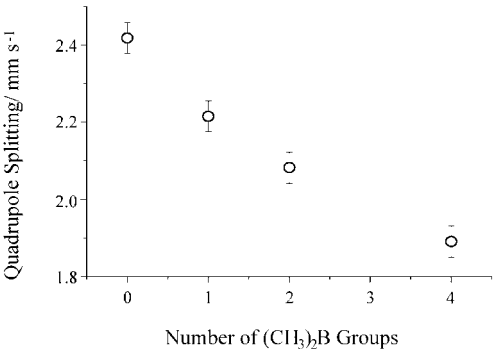

Figure 15. Variation of the quadrupole splitting [mm s^{-1}] at 90 K with the number of trimethylboron groups attached to the ferrocene backbones in compounds **4**, **10**, and **12**. The data point for $n=0$ is for parent ferrocene.

in the QS relative to ferrocene,[40] the Mössbauer data obtained here for **4a** (QS = 2.344 mm s^{-1}) and **10a** (QS = 2.339 mm s^{-1}) do not show any significant differences to FcH (QS = 2.418 mm s^{-1}).

As a means to understand the trends observed in the present Mössbauer measurements we used the qualitative Equation (1) established by Silver et al.,[39,40] which relates the quadrupole splitting of iron sandwich compounds to the iron 3d orbital population.

$$QS \sim 2p_2 - p_1 \quad (1)$$

Given an orientation of the Fe–COG bond in (substituted) ferrocenes along the z axis, p_1 represents the collective electron population of the $3d_{xz}$ and $3d_{yz}$ orbitals, and p_2 that of the $3d_{x^2-y^2}$ and $3d_{xy}$ orbitals. Essentially, an increase in p_1 corresponds to stronger π donation from the Cp ligands to the metal, which gives rise to negative contributions to QS, whereas a larger p_2 value indicates weaker δ backbonding from the metal to the ligand (i.e., more density remains at the iron atom), which leads to positive QS contributions with twice the magnitude relative to p_1.[44] Both p_1 and p_2 are sensitive to substitution at the Cp rings, whereas other iron valence orbitals ($3d_{z^2}$, 4s, and 4p) are considered to provide only negligible contributions to the QS.[39,40] Comparison of p_1^{FcH} and p_2^{FcH} obtained for FcH with the p_1 and p_2 populations in substituted ferrocenes leads to an expression for the corresponding changes in the QS according to Equation (2).

$$\Delta QS \sim \Delta p = 2(p_2 - p_2^{FcH}) - (p_1 - p_1^{FcH}) \quad (2)$$

To allow for a consistent comparison of iron d orbital occupations, we oriented all optimized structures from the TURBOMOLE BP86/TZVP/RI(TZVP-J)+COSMO calculations of the neutral species considered in the following by coordinate transformation in the same way (iron at the origin, Fe–COG along the z axis, C_{ipso} in the yz plane) and performed BP86/TZVP single-point calculations to obtain the orbital populations by means of natural population analysis (NPA), as implemented in the Gaussian program.[45,46]

We note in passing that populations obtained from a Mulliken analysis gave nearly identical results for Δp. The results obtained for Δp according to Equation (2) are listed in Table 4. Although it is evident that no unique proportionality factor connects the computed Δp values with the experimental QS data, the theoretical results qualitatively reproduce all experimentally observed trends when scaled uniformly by a factor of 2.052, obtained as the Δp/QS quotient for parent ferrocene. In line with the trend observed for measured QS values, successively smaller Δp_{scaled} values are found on going from FcH, **4**, **10**, to **12**. Also the counterintuitive finding mentioned above that the QS parameters for **4** and **4a** are rather similar ($\Delta QS = 0.035\ mm\,s^{-1}$), while the redox potentials differ by 0.49 V, is well reproduced by theory ($\Delta\Delta p_{scaled} = 0.037$ and $\Delta\Delta IE = 0.58$ eV). Further, for the **4a**/**10a** couple we find an identical Δp_{scaled} of 2.408 and a difference in ΔIE of 0.17 eV, which nicely fits the experimental findings ($\Delta QS = 0.005\ mm\,s^{-1}$ and a difference in redox potential of 0.26 V).

The opposite trends visible in the computed populations p_1 and p_2 (Table 4) allow for a qualitative interpretation of the binding situations in borylated ferrocenes: With increasing number of electron-withdrawing boryl substituents in the series FcH, **4**, **10**, **12**, the electron-acceptor capability of the Cp rings is gradually increased. Accordingly, in this series iron→Cp δ backbonding becomes stronger, as clearly indicated by the decreasing p_2 population. By the same token, the degree of Cp→iron π donation increases, which is reflected in the gradually increasing p_1 populations. The increase in p_1, however, amounts to merely one-third of the decrease in p_2. Thus, the changes in the electronic environment about iron visible in the QS values in this series are a consequence of a gradual improvement in δ backdonation. The improvements in π donation are significantly less pronounced.

Selected charges obtained from an NPA on neutral and ionized FcH, **1**, and the pyridine adduct **1a** are listed in Table 5. For the parent ferrocene, the removal of one electron leads to an increase of positive charge at the iron atom by about half an electron (0.45 e), and the group charges on both Cp rings increase uniformly by 0.28 e. Upon ionization of **1** the charge at iron increases by 0.43 e and that of the unsubstituted Cp_U ring by 0.22 e. The substituted Cp_S ring contributes only 0.14 e, and, significantly, 0.19 e are removed from the boron atom. This picture changes in the presence of a coordinating pyridine group (**1a**): while the charge on iron is again increased by 0.44 e, both Cp rings now contribute uniformly 0.23 e to the ionization, whereas only negligible changes occur for the charge at the boron atom. The pyridine group apparently compensates the higher charge deficiency at boron in the ion, as documented by its increased charge after ionization (by 0.09 e). Apparently, it is possible to decouple the boron atom quite efficiently from the ionization process by coordination with an N-donor base. The fact that the ionization potential of $[FcB(NH_2)_2]$ is very similar to that of parent ferrocene indicates that the same effect can also be accomplished by appropriate choice of the donor substituents at boron to efficiently compensate the electron deficiency at boron. The similarities in the computed charge distribution in neutral and cationic **1a** and FcH, respectively, indicate that such decoupling essentially leads to species with electronic (and electrochemical) properties very similar to parent ferrocene. This view is supported by the observed similarities in the QS for neutral FcH, **4a**, and **10a**. In this context, we attribute the finding of much lower ionization potentials compared to ferrocene or $[FcB(NH_2)_2]$ for the N-donor-substituted species **1a**, **4a**, and **10a** to the better distribution of charge over the entire, larger molecule. For all three species investigated, ionization leads to the removal of about half an electron from the iron atom, which is the largest observed change in charge distributions and quite independent of the presence of substituents or N-donor groups. We consider the substantial decrease in bending upon ionization observed for all relevant species (see Table 3) a consequence of the constantly in-

Table 5. Charges derived from NPA analysis of neutral and ionized FcH, **1**, and **1a**. The analysis was performed with the NBO routines implemented in Gaussian 03 at the BP86/TZVP level on optimized geometries obtained at the BP86/TZVP/RI(TZVP-J)+COSMO(CH_2Cl_2, $\varepsilon = 8.93$) level with the program TURBOMOLE.

	q(Fe)	$q(Cp_U)$[a]	$q(Cp_S)$[a]	q(B)	q(Py)[a]
FcH	0.18	−0.09	−0.09	–	–
FcH^+	0.63	0.19	0.19	–	–
Δq	0.45	0.28	0.28	–	–
1	0.21	0.00	−0.31	0.21	–
$\mathbf{1}^+$	0.64	0.22	−0.17	0.40	–
Δq	0.43	0.22	0.14	0.19	–
1a	0.20	−0.10	−0.35	−0.03	0.33
$\mathbf{1a}^+$	0.64	0.13	−0.12	−0.06	0.42
Δq	0.44	0.23	0.23	−0.03	0.09

[a] Group charges (sum over charges of all constituting C and H atoms) for the substituted (Cp_S) and unsubstituted (Cp_U) Cp ring systems.

Table 4. Correlation of the d orbital population at iron in substituted ferrocenes from natural population analyses and the experimentally determined quadrupole splitting (see text).

	$a_1'(d_{z^2})$	$e_1''(d_{xz})$	$e_1''(d_{yz})$	$e_2''(d_{x^2-y^2})$	$e_2''(d_{xy})$	p_1	p_2	Δp[a]	Δp_{scaled}[b]	QS
FcH	1.960	1.049	1.049	1.765	1.765	2.098	3.530	4.962	2.418	2.418
4	1.951	1.061	1.060	1.714	1.779	2.121	3.493	4.865	2.371	2.309
10	1.950	1.070	1.062	1.725	1.738	2.132	3.463	4.794	2.336	2.082
12	1.946	1.066	1.074	1.692	1.728	2.140	3.420	4.701	2.291	1.891
4a	1.959	1.048	1.057	1.767	1.756	2.105	3.523	4.942	2.408	2.344
10a	1.963	1.048	1.054	1.762	1.760	2.102	3.522	4.942	2.408	2.339

[a] Data computed according to Equation (2). [b] Proportionality factor 2.052 obtained as Δp/QS for parent ferrocene.

creased electron deficiency of the iron center in all ionized species, so that the electron deficiency at boron cannot be satisfied anymore by orbital or electrostatic interactions, which lead to bending in the neutral compounds (see below). We conclude from this section that, in the presence of a coordinating N-donor group, the boron atom does not contribute to the redistribution of charge in ionization processes, while its electron deficiency controls the ionization potential of substituted ferrocenes.

Analysis of the nature of bending in borylated ferrocenes: As a tentative explanation for the out-of-plane bending observed in borylated ferrocenes [$FcBX_2$], direct iron–boron interactions have been proposed, but previous experimental and theoretical work has been inconclusive in this respect.[47] To gain deeper insight into the nature of these hypothetical interactions, we performed a Bader analysis of the electron density topology for the model complex [$FcBH_2$] (**1**). Figure 16 shows the Laplacian of the electron density distribution in the Fe-C_{ipso}-B plane. Despite careful searching, no bond critical point between iron and boron was identified. In fact, the analysis unambiguously reveals that there is no common zero flux surface joining the iron and boron atomic basins. In other words, according to the quantum theory of atoms in molecules, there is no sign of covalent iron–boron bonding in **1**.

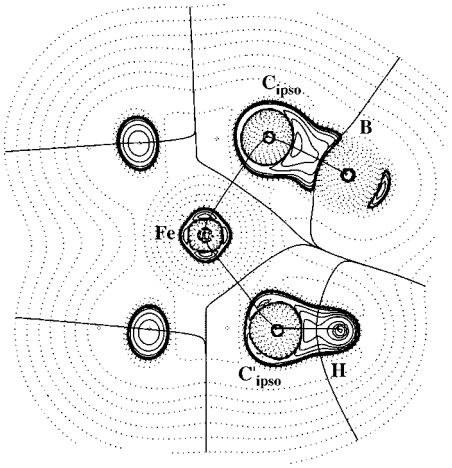

Figure 16. Laplacian of the electron density, zero-flux surface sections, and bond paths in the Fe-C_{ipso}-B plane of the model complex $FcBH_2$ (**1**) obtained from BP86/TZVP calculations.

To identify potential alternatives for understanding the nature of the experimental findings one must first assess the scale of the energetic consequences of the out-of-plane bending. To this end we performed relaxed potential energy scans for the bending in [$FcBH_2$] (**1**), and in the two fragments $[Fe(CpBH_2)]^+$ and $[CpBH_2]^-$. In these calculations we incrementally varied the bending angle Fe-C_{ipso}-B, which corresponds to a systematic variation of the dip angle α^*. The potential-energy curves obtained are shown in Figure 17. For the bending potential of the $[CpBH_2]^-$ fragment, we first note a rather shallow potential for the variation of α^*. In line with a low Cp–BH_2 out-of-plane bending

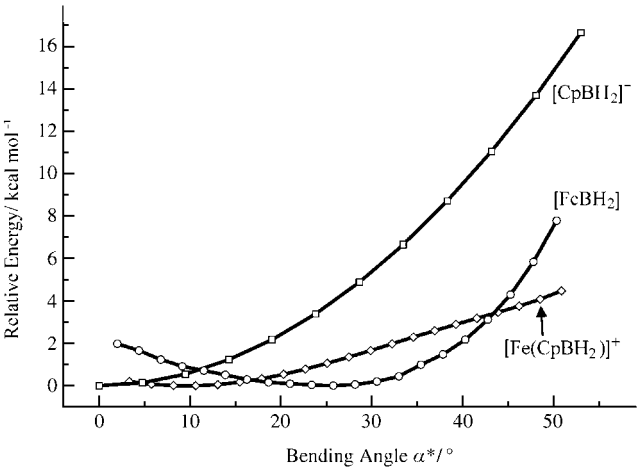

Figure 17. BP86/TZ2P (ADF) relaxed potential energy scan of the bending angle α^* in $[CpBH_2]^-$, $[Fe(CpBH_2)]$, and [$FcBH_2$] (**1**).

frequency (239 cm^{-1}), a deviation of 30° from the planar equilibrium geometry raises the energy by merely 4.5 kcal mol^{-1}. An even shallower potential results for the bending motion in $[Fe(CpBH_2)]^+$ (Figure 17). Its minimum structure exhibits a significant dip angle α^* of 7.5°, but it is stabilized by only 0.2 kcal mol^{-1} with respect to the planar geometry. Correspondingly, an α^* of +30° leads to a very small energy increase of 2.0 kcal mol^{-1}, and the associated out-of-plane bending frequency is significantly lowered (130 cm^{-1}). Also for **1** an equally weak bending potential results (Figure 17). In the optimized minimum structure, the boryl group is now bent substantially towards the iron center by about 25°. The energy difference to the planar structure, however, is again only 2.0 kcal mol^{-1}. Frequency analysis on minimum **1** gave 106 cm^{-1} for the out-of-plane bending vibration. Starting from the minimum, a further increase of α^* leads to a somewhat steeper repulsive potential than in $[Fe(CpBH_2)]^+$ due to the presence of the second Cp^- ring. However, even the heavily distorted structure at the end of the scan ($\alpha^* = 50°$, Fe–B 2.240 Å) is just 8 kcal mol^{-1} higher in energy. Taken together, from this subsection it becomes immediately clear that the energetic effects underlying the experimentally observed deviations from planarity for the borylated ferrocenes under study are of rather small magnitude.

To further understand the changes in electronic structure accompanying bending, we performed NPAs for several points along the scan of **1** (Table 6). According to the NPA a small amount of charge is transferred onto the BH_2 group as it is bent towards the iron atom, for example, 0.09 e in the minimum structure ($\alpha^* = 26°$) and 0.22 e at the limit of the scan ($\alpha^* = 45°$). This charge stems mainly from the C_{ipso} atom and the unsubstituted Cp ring, which donates up to 0.1 e to the boron group. The iron atom is hardly involved at all in the overall charge redistribution, which is in line with the finding of rather constant IS values in the Mössbauer spectra of FcH and **4** presented above. Thus, bending results

Table 6. NPA analyses of several points along the angle bending scan of **1** (BP86/TZVP). Charge differences relative to the planar structure are given.

α^*	45°	40°	35°	31°	26°	21°	16°	12°	7°	2°	q[b]
Cp[a]	0.10	0.08	0.06	0.05	0.03	0.02	0.01	0.01	0.00	0.00	0.00
$CpBH_2$[a]	−0.04	−0.03	−0.03	−0.02	−0.02	−0.01	−0.01	−0.01	0.00	0.00	−0.21
C_{ipso}	0.15	0.12	0.10	0.08	0.06	0.05	0.03	0.02	0.01	0.00	−0.37
BH_2[a]	−0.22	−0.18	−0.15	−0.12	−0.09	−0.07	−0.05	−0.03	−0.01	0.00	0.10
Fe	−0.06	−0.05	−0.03	−0.02	−0.02	−0.01	−0.01	0.00	0.00	0.00	0.21

[a] Charge differences based on group charges given as the sum of charges of all constituting atoms. [b] Total charges obtained for the minimum structure.

essentially in a polarization of charge within the $Cp-BH_2$ moiety.

Some degree of iron–boron interaction can be identified in a Wiberg bond-order analysis:[48] The Fe–B bond order increases from 0.12 (planar structure) to 0.18 in the minimum structure to 0.22 at the limit of $\alpha^* = 45°$. To put this result into perspective we note that the $Fe-C_{ipso}$ bond order is somewhat larger (0.28), but remains constant upon bending. According to these results, the iron–boron interaction in the minimum structure amounts to about two-thirds of the iron–carbon interaction. Indeed, similar findings in the context of Mayer bond orders led Appel et al. to propose a direct iron–boron bonding interaction.[22] In the analysis of natural bond orbitals (NBOs), however, we do not find any particular orbital corresponding to a direct Fe–B bond. Instead, after involving an orbital localization procedure based on NBOs, the only significant interaction of these two atoms is found in a three-center natural localized molecular orbital (NLMO) distributed over Fe, C_{ipso}, and B (Figure 18). Note,

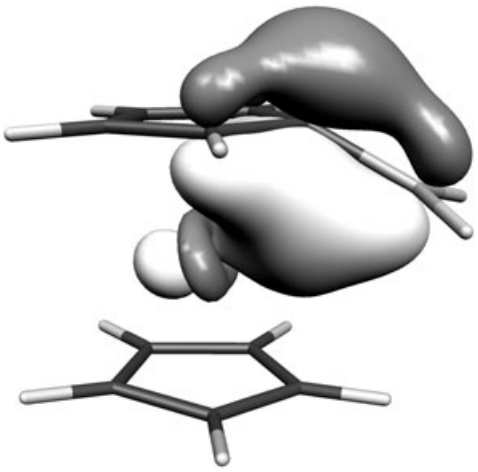

Figure 18. Three-center bonding NLMO involving Fe, C_{ipso}, and B obtained from an NBO analysis for the model complex **1**.

however, that we found in additional calculations that the use of different methods or basis sets results in somewhat different orbital compositions, which clearly indicates some ambiguity in the concept of orbital localizations within the NBO framework. Hence, notwithstanding the intuitively appealing outcome, this result cannot be seen as a rigorous basis for interpretation of the binding situation. All in all, also in view of our findings arising from the Bader analysis, we refrain from correlating the NBO results with direct covalent iron–boron bonding at this point. The bonding situation appears to be better described as a strongly delocalized, multicenter bonding interaction involving Fe, C_{ipso}, and B of the $Cp-BH_2$ moiety.

A comparison of canonical Kohn–Sham molecular orbitals of the parent ferrocene with those of its borylated derivative **1** reveals some interesting trends in the energetic ordering. Figure 19 shows a qualitative correlation of valence orbitals

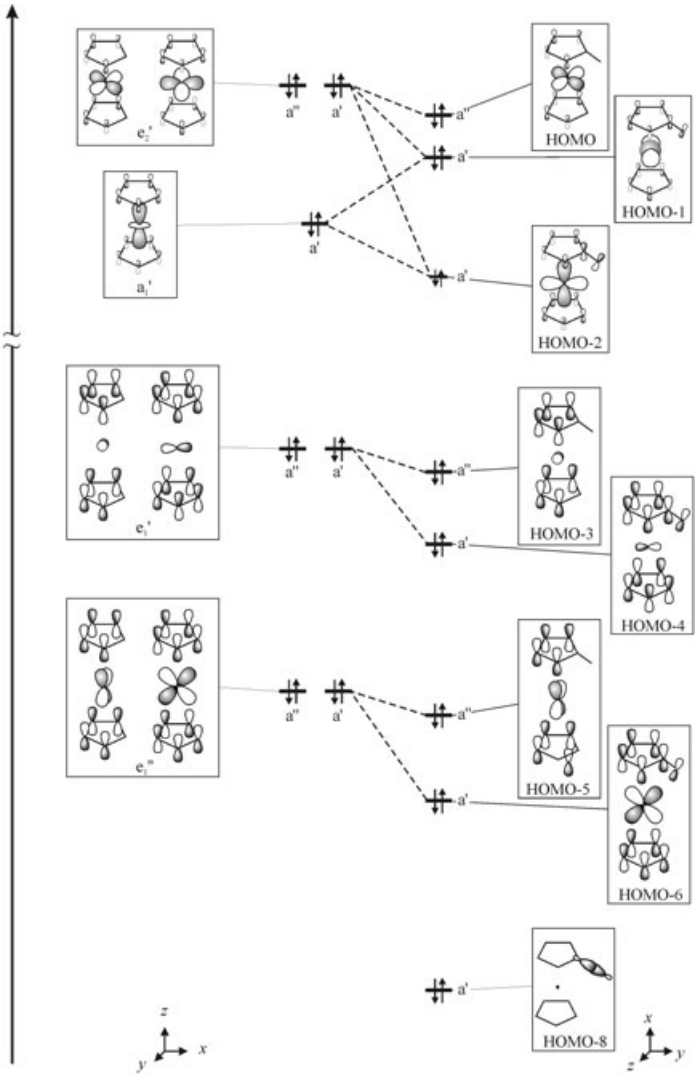

Figure 19. Correlation diagram for selected MOs in ferrocene (C_s representation of the D_{5h}-symmetric MOs of ferrocene, left) and **1** (right).

in the D_{5h} symmetric minimum structure of ferrocene with those of **1**, for which C_s symmetry was enforced to facilitate the analysis. Apart from a general energetic lowering of the orbitals in **1** induced by the presence of the boryl group, we note an additional stabilization of all a′ relative to a″ valence orbitals. In **1**, the formally unoccupied p_x orbital at boron (i.e., the p orbital perpendicular to the plane of the adjacent Cp ring) and the C_{ipso}–B bond orbital are symmetric with respect to the molecular mirror plane and thus of a′ symmetry. In particular the HOMO−2 a′ orbital experiences a strong stabilization, which can be attributed to a constructive interaction of the d_{xy} orbital at iron with the p_x orbitals making up the local π bond between C_{ipso} and B. Similar interactions can be identified for the a′ symmetric orbitals HOMO−1 and HOMO−6. Notably, the unsubstituted Cp ring participates significantly in the Aufbau of the HOMO−4 orbital (Figure 20), such that in principle a direct

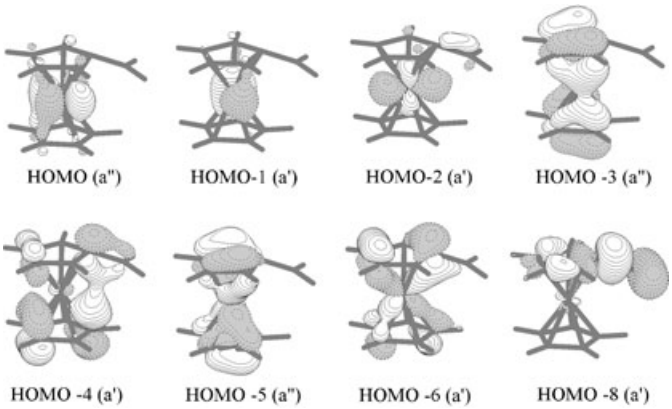

Figure 20. Molden[114] plots of selected valence MOs for **1**.

constructive interaction between the formally empty p_x orbital at boron with the C'_{ipso} center of the unsubstituted Cp ring is involved. Here, the iron contributes only a small amount of antibonding 4p character. From Figure 19 it becomes clear that this through-space type of interaction in **1** arises as a mere consequence of the orbital structure of parent ferrocene, in which a similar type of delocalized interaction is present in the corresponding a′-symmetric orbitals. In HOMO−4 and HOMO−6 of **1** this delocalization is visibly extended to involve the boryl π system. This picture lends weight to the interpretation of strongly delocalized orbital interactions being responsible for the bending in borylated ferrocenes. The only localized direct iron–boron interaction is visible in HOMO−2, with only minor contributions of the boron p_x orbital.

A Walsh diagram illustrating the changes in MO energies upon systematic variations of α^* in **1** is shown in Figure 21. Consistent with the discussion above, we note a much stronger dependence on α^* for the symmetric a′ orbitals than for a″ orbitals. These effects are particularly prominent for the HOMO−2 orbital, which is strongly stabilized upon bend-

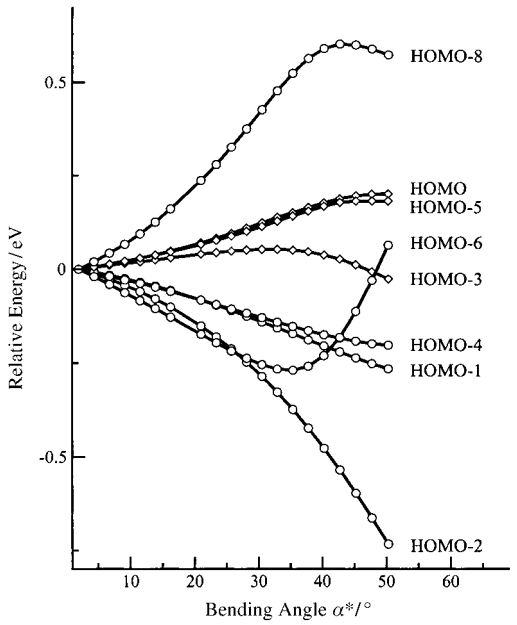

Figure 21. Walsh diagram illustrating the changes in MO energies upon systematic variation of α^* in **1** (obtained at the BP86/TZ2P level). See Figures 5 and 6 for the numbering scheme of orbitals.

ing. The HOMO−8 orbital, on the other hand, experiences a similarly strong destabilization with increasing α^*. While these two orbitals dominate the picture for the $\alpha^* = 50°$ limit of the scan, the stabilization of the HOMO−6 orbital is equally strong as that of HOMO−2 in the minimum structure ($\alpha^* = 26°$). In summary, the qualitative picture arising from this analysis intuitively renders these two orbitals the root of attractive interactions responsible for the observed bending. This stabilization is evidently counterbalanced by the destabilization of the C_{ipso}–B σ-bonding orbital (HOMO−8) upon bending.

As an extension of these qualitative arguments, which are essentially based on an orbital overlap picture, we performed an energy partitioning analysis (EPA) as implemented in the ADF program. For this analysis we divided **1** into the fragments $[FeCp]^+$ and $[CpBH_2]^-$. Both are treated as singlet states and the analysis was performed under C_s symmetry constraints. The changes in the relative energy contributions upon systematic variations of α^* shown in Figure 22 clearly reveal that stabilizing orbital contributions to the bending arise from the a′ set of orbitals, while a″ contributions remain essentially constant and thus cannot be responsible as a driving force for bending. This is in agreement with the qualitative conclusions drawn above from the Walsh diagram. A similarly strong contribution originates in the electrostatic term E_{ELSTAT}. Destabilizing contributions stem from the Pauli energy term E_{PAULI} and from the preparation energy. The latter term arises almost completely from distortion of the $[CpBH_2]^-$ fragment in the complex. From this analysis we conclude that the driving force for bending is rooted in the stabilization of a′ orbitals as well as in significantly enhanced electrostatic interactions.

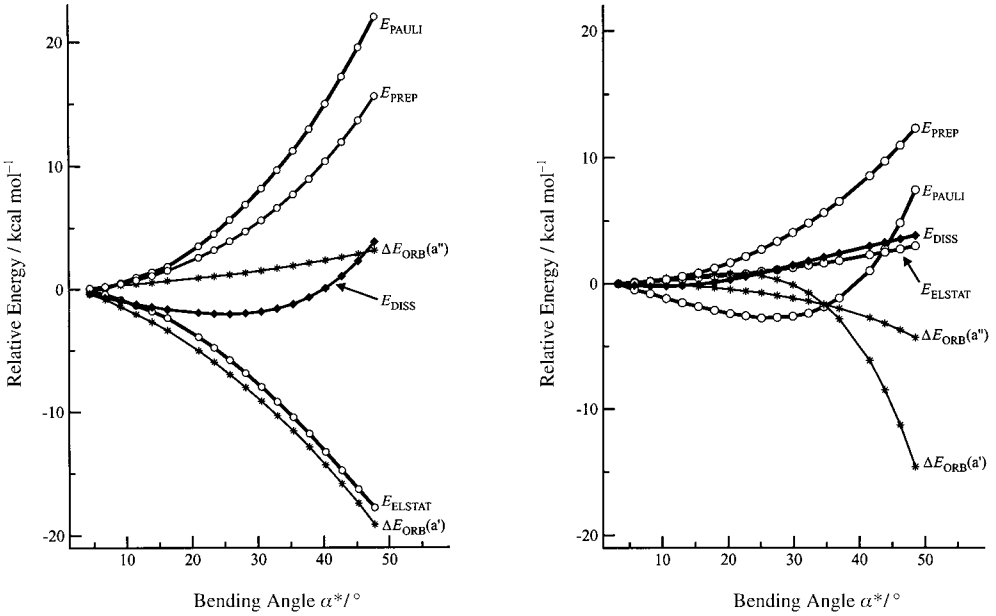

Figure 22. Differential changes in energy contributions from the energy partitioning analysis (EPA) upon variation of α^* in **1** (left) and $[FeCpBH_2]^+$ (right) based on BP86/TZ2P results.

To assess the energetic contributions of the second Cp ring to the bending potential, we also performed a corresponding energy partitioning analysis for the $[FeCpBH_2]^+$ subunit, which was divided into $CpBH_2^-$ and Fe^{2+}. For the latter fragment, the closed shell $(d_{z^2})^2$, $(d_{x^2-y^2})^2$, and $(d_{xz})^2$ reference electron configuration was employed, which constitutes a highly excited state for the bare Fe^{2+} ion, but serves here as a reasonable valence state of Fe^{2+} in the $[FeCpBH_2]^+$ complex to obtain relative EPA energy contributions during a scan of α^*. For the evaluation of the preparation energy term E_{PREP}, however, the correct $3d^6$ (^5D) configuration was employed.[49] The results are shown in Figure 22. Interestingly, we find entirely different trends for the respective energy components compared to **1**. Most strikingly, the differential E_{ELSTAT} contributions here do not add to the stabilizing factors of the bending. In fact, in sharp contrast to our findings for **1**, up to $\alpha^* = 30°$ the differential Pauli contributions are the only stabilizing factor. From $\alpha^* = 35°$ onwards the $\Delta E_{ORB}(a')$ term is strongly stabilizing, the E_{PAULI} term becomes destabilizing, whereas $\Delta E_{ORB}(a'')$ and E_{ELSTAT} show only negligible contributions. The E_{PREP} term is destabilizing along the entire scan. While the reasons for the pronounced qualitative differences in the EPA results for **1** and its $[FeCpBH_2]^+$ subunit are hard to rationalize (this is particularly true for the peculiar shape of the E_{PAULI} curve), we note that the overall differential contributions of all constituent energy terms are less than 5 kcal mol^{-1} for the range of $\alpha^* = 0$–$30°$ and are thus of limited importance. On the basis of these analyses, however, we feel safe to state that the second Cp ring in **1** contributes significant electrostatic factors favoring bending of the boryl substituent.

In the overall picture arising from our analysis, the bending cannot be understood in terms of direct bonding interactions involving the boryl group and the iron center; on the basis of a Bader electron topology analysis we can safely exclude such a direct bond. Based on in-depth investigations on our computational model for borylated ferrocene **1**, our analysis rather indicates that the bending is rooted in several contributions. We identified two apparently cooperative factors giving rise to bending in this class of organometallic compounds: Two MOs of a′ symmetry (HOMO−2 and HOMO−6) experience a substantial lowering of energy upon bending. These orbitals represent covalent contributions to bending involving 1) a strongly delocalized interaction of both Cp rings, which is effectively mediated by the d_{xy} orbital at iron (HOMO−6); and 2) a rather localized interaction of the $d_{x^2-y^2}$ orbital at iron and the C_{ipso}–B π system (HOMO−2). Both orbitals, however, are already present in parent ferrocene and contain only limited contributions from the formally empty p_x orbital of the boron substituent. The most significant interaction involving the boron p_x orbital as part of the C_{ipso}–B π system is present in HOMO−4, which represents a delocalized through-space interaction with the second Cp ring without involvement of iron orbitals; a minor contribution of the iron $4p_y$ orbital to this MO is antibonding in nature. HOMO−4, however, does not experience any significant energy lowering with increasing dip angle α^* and is therefore unlikely to be the origin of the observed bending. As a second and, according to the EPA, equally important factor we identified electrostatic interactions, which are enhanced substantially upon bending. These interactions depend essentially on the presence of a second Cp ring. Contrary to chemical intuition, NPA analy-

ses indicate that bending is not accompanied (or caused) by any significant charge transfer from the metal to the electron-deficient boron center. Instead, a reorganization of charge within the $CpBH_2^-$ moiety is observed which leads to a flow of charge from the C_{ipso} center to the BH_2 group. The NPA results indicate a constant electron density about the iron center which is unaffected by the electronic situation of the boryl substituent. This picture is in line with the IS values measured in our Mössbauer study on the present set of compounds bearing one, two, or four BMe_2 groups.

Conclusion

This paper presents a joint crystallographic, electrochemical, and Mössbauer spectroscopic study on selected derivatives of mono-, di-, and tetraborylated ferrocenes $[FcB(R^1)(R^2)]$, 1,1′-$[fc\{B(R^1)(R^2)\}_2]$ (R^1, R^2 = Br, Me, OH, OMe), and 1,1′,3,3′-$[Fe\{C_5H_3(BMe_2)_2\}_2]$. The results obtained are put face-to-face with detailed DFT calculations, which include the hypothetical parent compound $[FcBH_2]$, even though it is not experimentally accessible. As a common feature of all molecular structures investigated, the three-coordinate boryl substituents are bent out of the plane of the adjacent cyclopentadienyl ring towards the iron atom. For a quantitative assessment of ligand bending we used the dip angle $\alpha^* = 180° - \alpha$, where α is defined as the angle COG-C_{ipso}-B (COG: geometric center of the Cp carbon atoms). As a general rule, α^* tends to decrease with decreasing Lewis acidity of the boron atom, as well as with increasing degree of borylation at the ferrocene core. A similar structural motif is also clearly visible in all structures obtained from quantum chemical calculations, even though we do not always find a full quantitative agreement between theory and experiment. Nevertheless, the systematic trend in α^* values as a function of the Lewis acidity of the boryl groups is well reproduced by density functional calculations. This leads to the conclusion that ligand bending is not merely an artifact of crystal packing, but is rooted in the electronic structure of the individual molecules. However, since the potential-energy surface associated with changes in the dip angle is apparently very shallow, solid-state effects may well have some non-negligible influence on α^*, which in turn may account for the deviations between theory and experiment visible in the quantitative description of the phenomenon.

At first, we hypothesized about Cp–$B(R^1)(R^2)$ bending as originating from a direct interaction between filled d-type orbitals at iron and the empty p orbital at boron. However, a Bader analysis of the electron density topology for the model complex $[FcBH_2]$ (**1**), which exhibits a pronounced bending of $\alpha^* = 26.5°$ at the BP86/TZVP level, clearly shows that there is no direct iron–boron bonding in **1**. Further detailed analysis rather reveals that two cooperative factors exist that are responsible for ligand bending. We identified several orbital interactions of delocalized nature that involve the formally empty p orbital at the boryl substituent, C_{ipso} of the adjacent Cp ring, d orbitals at iron, and also a significant through-space interaction with the second Cp ring. As a second and, according to our analysis, equally important factor, we identified electrostatic interactions, which are enhanced substantially upon bending and which depend critically on the presence of the second Cp ring.

Apart from the structural features of ferrocenylboranes, we are particularly interested in their electrochemical behavior and potential use for the development of novel electron-transfer reagents. Thus, the series $[FcBMe_2]$ (**4**, $E^{0\prime} = +0.09$ V vs FcH/FcH^+), 1,1′-$[fc(BMe_2)_2]$ (**10**, $E^{0\prime} = +0.26$ V) and 1,1′,3,3′-$[Fe\{C_5H_3(BMe_2)_2\}_2]$ (**12**, $E^{0\prime} = +0.39$ V) was investigated by cyclic voltammetry. Our study reveals that the introduction of BMe_2 substituents into the ferrocene core increases the oxidation potential of the central iron atom. This anodic shift, which is apparently additive, can be attributed to the π-electron-withdrawing nature of three-coordinate boryl groups. Most importantly, the addition of 4-dimethylaminopyridine (DMAP; 1 equiv for **4**, 2 equivs for **10**) with subsequent B–N adduct formation does not just neutralize this effect but leads to a cathodic shift of the Fe^{II}/Fe^{III} redox transition far beyond the half-wave potential of parent ferrocene [$E^{\circ\prime}$(**4a**) = −0.40 V, $E^{\circ\prime}$(**10a**) = −0.66 V vs FcH/FcH^+]. It is noteworthy that the diadduct **10a** is as easy to oxidize as decamethylferrocene, which is one of the most prominent electron donors for the generation of organometallic charge-transfer salts. Cyclic voltammetry was augmented by DFT calculations, including solvent simulations, on the adiabatic ionization energies (IEs) of **4**, **10**, **12**, **4a**, and **10a**. In all these cases we find an excellent correlation between the experimentally obtained $E^{\circ\prime}$ values and the calculated IE data.

To get further insight into the charge-density flow within the ferrocene backbone upon introduction of BMe_2 or BMe_2–DMAP substituents, the series **4**, **10**, **12**, **4a**, and **10a** was also investigated by Mössbauer spectroscopy. As expected, only negligible differences in the isomer shift (IS) of the borylated species and parent ferrocene are observed. The quadrupole splittings (QS), however, become significantly smaller upon going from **4** (2.309(4) $mm\,s^{-1}$) to **10** (2.082(4) $mm\,s^{-1}$) and **12** (1.891(4) $mm\,s^{-1}$). These results are in agreement with previous findings which indicated that electron-withdrawing substituents at ferrocene cause a decrease in QS. Electron-donating substituents, on the other hand, tend to cause an increase in the quadrupole splitting relative to ferrocene ($QS = 2.37\ mm\,s^{-1}$). In contrast to a priori expectations, the QS values of **4a** (2.344(3) $mm\,s^{1}$) and **10a** (2.339(4) $mm\,s^{-1}$) do not differ significantly from that of ferrocene despite the low oxidation potentials and ionization energies found for these B–N adducts. Based on an empirical correlation between the d orbital populations and the QS, we have rationalized the experimentally observed trends in the QS data for these species in terms of changes in the Cp–Fe bonding features of ferrocene resulting from different degrees of borylation. Furthermore, by comparison with parent ferrocene, we found for the model compounds **1** and the pyridine derivative **1a** that the ionization process removes about half an electron from the iron atom, which is the largest charge difference uniformly for all

three species. Notably, the charge of the boron atom in three-coordinate **1** is increased by 0.2 e upon ionization, whereas no change is seen at boron after ionization of **1a**. With this result, we interpret the experimentally observed trends in the redox potentials as follows: for borylated ferrocenes such as **4**, **10**, and **12** the electron deficiency at the three-coordinate boron center(s), which can be modulated by choice of appropriate substituents at boron, leads to an increase in the ionization potential of the complexes with respect to ferrocene. This is a result of the π-electron-withdrawing nature of the boryl substitutents. In the presence of coordinating Lewis bases or strong π donors at boron (e.g., $[FcB(NH_2)_2]$), however, the boron atom is effectively decoupled from the ionization process, and the redox potentials of the resulting complexes are equal to or even lower than that of ferrocene itself. Hence, cyclic voltammetry can be regarded as an analytical tool for the identification of base adducts in such complexes. Furthermore, given the constantly good agreement (within 0.1 V) between theory and experiment observed for all species under investigation, it appears possible to predict the redox properties of related complexes a priori, which opens the way to a rational design of tailor-made redox-active ferrocenoid complexes with fine-tuned redox potentials. However, careful benchmarking is always required to obtain reliable results. In the present study we have documented by comparison with high-level post-HF results that the DFT approximations presently in use can fail miserably in the description of N-donor/B-acceptor bond strengths. Notwithstanding these problems, which need to be identified for every new class of molecules by adequate scrutiny prior to any predictive application, we clearly demonstrated that DFT calculations are a reliable tool with predictive capabilities for the description of demanding electronic situations as are present in borylated ferrocenes with their very subtle electronic and/or structural properties.

Experimental Section and Computational Methods

General remarks: All reactions and manipulations of air-sensitive compounds were carried out in dry, oxygen-free argon using standard Schlenk ware. Solvents were freshly distilled under N_2 from Na/benzophenone (benzene, toluene) or Na/Pb alloy (hexane) prior to use. NMR: Bruker DPX 400, Bruker DPX 250. ^{11}B NMR spectra are reported relative to external $BF_3{\cdot}Et_2O$. Unless stated otherwise, all NMR spectra were recorded at ambient temperature; abbreviations: s = singlet, d = doublet, tr = triplet; vtr = virtual triplet; n.o. = signal not observed; n.r. = multiplet expected but not resolved. $FcSnMe_3$[25] and compounds **2**,[1] **3**,[1] **4**,[1] **4a**,[5] **8**,[2] **10**,[2] and **10a**[5] were synthesized according to literature procedures.

Preparation of 5: Triethylamine (0.19 g, 1.88 mmol) and water (0.10 g, 5.55 mmol) were added dropwise with stirring at ambient temperature to a solution of **3** (0.54 g, 1.86 mmol) in benzene (6 mL). The solution was stirred for 1 h. After the benzene had been removed in vacuo, hexane (15 mL) was added to the residue, and the resulting slurry cooled to −40 °C for 6 h. After filtration from triethylammonium bromide, all volatiles were driven off from the filtrate under reduced pressure to leave behind a pale yellow microcrystalline solid. Yield: 0.19 g (45 %). Single crystals of **5** formed serendipitously from the crude oily compound $[FcBMe_2]$ (**4**) upon prolonged exposure to air. ^{11}B NMR (128.4 MHz, $CDCl_3$): $\delta = 49.6$ ppm ($h_{1/2} = 250$ Hz); ^{1}H NMR (250.1 MHz, $CDCl_3$): $\delta =$ 0.62 (s, 3H; CH_3), 4.10 (s, 5H; C_5H_5), 4.33, 4.45 (2 vtr, $^3J(H,H) = {}^4J(H,H) = 1.8$ Hz, 2×2H; C_5H_4), 4.92 ppm (s, 1H; OH); ^{13}C NMR (62.9 MHz, $CDCl_3$): $\delta =$ n.o. (CH_3), 68.5 (C_5H_5), 72.9, 73.3 ppm (C_5H_4), n.o. (C_5H_4-ipso); elemental analysis calcd (%) for $C_{11}H_{13}BFeO$ (227.87): C 57.98, H 5.75; found: C 57.51, H 5.49.

Preparation of 6: $MeOSiMe_3$ (1.56 g, 14.97 mmol) was added by syringe to a suspension of **2** (2.13 g, 5.99 mmol) in pentane (20 mL) at −78 °C. The mixture was allowed to warm to room temperature and stirred for 30 min. All volatiles were removed in vacuo. Distillation of the crude product gave **6** as an orange solid. Yield: 1.45 g (94 %). X-ray quality crystals were obtained by sublimation under reduced pressure. ^{11}B NMR (128.4 MHz, $CDCl_3$): $\delta = 30.0$ ppm ($h_{1/2} = 160$ Hz); ^{1}H NMR (250.1 MHz, $CDCl_3$): $\delta = 3.75$ (s, 6H; CH_3), 4.15 (s, 5H; C_5H_5), 4.38, 4.44 ppm (2 n.r., 2×2H; C_5H_4). ^{13}C NMR (100.6 MHz, $CDCl_3$): $\delta = 52.0$ (CH_3), 68.5 (C_5H_5), 71.8, 74.4 ppm (C_5H_4), n.o. (C_5H_4-ipso); elemental analysis calcd (%) for $C_{12}H_{15}BFeO_2$ (257.90): C 55.88, H 5.86; found: C 55.51, H 5.58.

Preparation of 7: A solid mixture of **2** (0.07 g, 0.20 mmol) and $[FcSnMe_3]$ (0.07 g, 0.20 mmol) was dissolved in C_6D_6 (1 mL) in an NMR tube, which was cooled to liquid-nitrogen temperature, evacuated, and sealed. The reaction mixture was allowed to warm to ambient temperature, whereupon a colorless precipitate formed (Me_3SnBr). The NMR tube was turned bottom up, and the solid separated from the mother liquid by centrifugation. After NMR investigation, the NMR tube was opened under inert gas, and all volatiles removed in vacuo to yield a red microcrystalline solid. Yield: 0.06 g (65 %). X-ray quality crystals were obtained from toluene upon slow evaporation of the solvent in vacuo. ^{11}B NMR (128.4 MHz, C_6D_6): $\delta = 55.3$ ppm ($h_{1/2} = 450$ Hz); ^{1}H NMR (250.1 MHz, C_6D_6): $\delta = 4.00$ (s, 10H; C_5H_5), 4.43, 4.71 ppm (2 vtr, $^3J(H,H) = {}^4J(H,H) =$ 1.8 Hz, 2×4H; C_5H_4); ^{13}C NMR (62.9 MHz, C_6D_6): $\delta = 70.2$ (C_5H_5), 75.4, 77.0 ppm (C_5H_4), n.o. (C_5H_4-ipso). Compound **7** is very sensitive to air and moisture; a correct elemental analysis was therefore not obtained.

Preparation of 11: $MeOSiMe_3$ (3.78 g, 36.27 mmol) was added by syringe to a solution of **8** (3.86 g, 7.35 mmol) in toluene (30 mL) at −78 °C. The mixture was allowed to warm to room temperature and stirred for 30 min. All volatiles were removed in vacuo. X-ray quality crystals were obtained by recrystallization of the crude product from hexane. Yield: 1.79 g (74 %). ^{11}B NMR (128.4 MHz, $CDCl_3$): $\delta = 30.0$ ppm ($h_{1/2} =$ 210 Hz); ^{1}H NMR (250.1 MHz, $CDCl_3$): $\delta = 3.74$ (s, 12H; CH_3), 4.35, 4.42 ppm (2 vtr, $^3J(H,H) = {}^4J(H,H) = 1.5$ Hz, 2×4H; C_5H_4); ^{13}C NMR (100.6 MHz, $CDCl_3$): $\delta = 51.9$ (CH_3), 72.1, 74.7 ppm (C_5H_4), n.o. (C_5H_4-ipso); elemental analysis calcd (%) for $C_{14}H_{20}B_2FeO_4$ (329.77): C 50.99, H 6.11; found: C 50.73, H 5.92.

Preparation of 12: Neat 1,1′,3,3′-$[Fe\{C_5H_3(BBr_2)_2\}_2]$[26] (0.70 g, 0.81 mmol) was cooled to −30 °C. Neat $SnMe_4$ (1.30 g, 7.27 mmol) was added with gentle stirring by syringe. The mixture was allowed to warm to room temperature and heated to 80 °C for 2 h. All volatiles were removed in vacuo while the mixture was still hot. Sublimation of the residue at 60 °C/10^{-3} Torr gave dark red X-ray quality crystals. Yield: 0.25 g (89 %); ^{11}B NMR (128.4 MHz, C_6D_6): $\delta = 74.8$ ppm ($h_{1/2} = 310$ Hz); ^{1}H NMR (400.0 MHz, C_6D_6): $\delta = 0.88$ (s, 24H; CH_3), 4.48 (d, 4H; $^4J(H,H) = 1.2$ Hz, C_5H_3), 4.56 ppm (tr, $^4J(H,H) = 1.2$ Hz, 2H; C_5H_3); ^{13}C NMR (100.6 MHz, $CDCl_3$): $\delta = 11.5$ (CH_3), 81.1, 82.4 ppm (C_5H_3), n.o. (C_5H_3-ipso); elemental analysis calcd (%) for $C_{18}H_{30}B_4Fe$ (345.51): C 62.57, H 8.75; found: C 62.05, H 8.51.

X-ray crystal structure analyses: Crystals of **3**, **4**, **4a**, **5**, **6**, **7**, **9**, and **11** were measured on a STOE IPDS II two-circle diffractometer with graphite-monochromated $Mo_{K\alpha}$ radiation. An empirical absorption correction was performed by using the MULABS[50] option in the program PLATON.[51] Compound **12** was measured on a Siemens SMART CCD diffractometer with graphite-monochromated $Mo_{K\alpha}$ radiation. A numerical absorption correction was performed by using the program SHELXTL.[52] All structures were solved by direct methods using the program SHELXS[53] and refined against F^2 with full-matrix least-squares techniques with the program SHELXL.[54] All non-hydrogen atoms were refined with anisotropic displacement parameters. Hydrogen atoms, except those of the disordered methyl group in **3**, were located by difference Fourier synthesis and refined using a riding model. The methyl and OH groups were allowed to rotate but not to tip. The methyl group and

the Br atom of **3** are disordered. The Br/CH_3 ratio is 0.681(3)/0.319(3) on one position and 0.319(3)/0.681(3) on the other. Similarity restraints were used for the displacement parameters of these atoms. CCDC-242167 (**3**), CCDC-242165 (**4**), CCDC-242168 (**4a**), CCDC-242164 (**5**), CCDC-242170 (**6**), CCDC-242169 (**7**), CCDC-242166 (**9**), CCDC-242171 (**11**), and CCDC-242172 (**12**) contain the supplementary crystallographic data for this paper. These data can be obtained free of charge via www.ccdc.cam.ac.uk/conts/retrieving.html (or from the Cambridge Crystallographic Data Centre, 12 Union Road, Cambridge CB21EZ, UK; fax: (+44) 1223-336-033; or deposit@ccdc.cam.uk).

Electrochemical measurements: Cyclic voltammetry was performed in CH_2Cl_2 containing NBu_4PF_6 (0.1 mol dm^{-3}) as supporting electrolyte. All potentials are relative to the FcH/FcH^+ redox couple. Voltammetric scans were referenced by addition of a small amount of ferrocene as internal standard at an appropriate time of the experiment. The cell for electrochemistry measurements was designed as detailed in ref. [55]

Mössbauer spectroscopy: The details of ^{57}Fe temperature-dependent Mössbauer spectroscopy have been described earlier.[56–58] In the present study, due to the air and moisture sensitivity of the compounds, sample transfer to perspex sample holders, lubricated with high-temperature silicone grease and sealed with O-rings, was effected in an inert-atmosphere glove box (VAC model DLX-001-S-P) having a oxygen partial pressure of less than 0.5 ppm and less than 1 ppm H_2O. Since **4** is a low-melting semisolid at room temperature, and **10** is a liquid, both compounds were transferred by capillary pipette. Compounds **4a** and **10a** were transferred as neat microcrystalline solids. The filled and sealed sample holders were removed from the glove box, immediately cooled to liquid-nitrogen temperature, and then placed into the Mössbauer spectrometer precooled to 90 K. Data accumulation (in the first instance) was effected in a warming mode as discussed above. All isomer shifts are reported with respect to the centroid of a room-temperature α-Fe absorber spectrum, which was also used for spectrometer calibration.

Quantum chemical calculations: Results of an incipient systematic benchmark study is provided as Supporting Information. Quantum chemical calculations were carried out at various levels by means of the programs Gaussian 03,[59] Turbomole,[60–64] Molpro,[65] and ADF.[66,67] At the density functional level we employed the standard BP86[68,69] functional as well as the HCTH407[70–72] functional of Boese et al., which was newly implemented in the Gaussian 03 program (HCTH for short). Both of these functionals are based on the generalized gradient approximations (GGA) and can make use of the resolution of identity (RI) approximation,[73–77] which usually improves the computational efficiency and scalability with system size substantially. At the hybrid DFT level we employed the B3LYP functional[78,79] and the B98 functional of Schmider and Becke.[80,81] All Gaussian and Turbomole calculations were done in combination with the SVP and TZVP basis sets of Ahlrichs et al.[82,83] In RI computations with the Gaussian program we used the small DGA1 Coulomb density fitting basis available in the basis set library.[84] Calculations on redox potentials were performed at the BP86(RI) level with the Turbomole program, employing its very efficient implementation of the COSMO continuum model[85] to account for solvation effects (solvent dichloromethane, dielectric constant at room temperature $\varepsilon = 8.93$). The TZVP basis set was used for B, C, N, O, F, and H atoms. For Cl, Br, and I atoms the relativistic effective core potentials of Dolg et al.[86,87] were used. The respective TZV-type standard basis sets for the latter atoms were each augmented by one d polarization function available in the Turbomole basis set libraries. For all atoms, the TZVP-J Coulomb fitting basis was used. Note that we report in the tables ionization energies obtained from total energy differences because we cannot account for thermochemical corrections to obtain ΔG values due to the lack of analytic second derivatives in the COSMO calculations. We therefore provide only a qualitative assessment of the electrochemical conditions, and accordingly we report computed ionization energies in electron volt, whereas the differences in redox potentials obtained in electrochemical measurements are given in volt and relate to free energy differences. A gas-phase calculation on **4** at the BP86/TZVP/RI(DGA1) level, that is, without solvent simulation, however, yields zero-point vibrational energy and thermal contribution effects (ΔG at 298 K) on the adiabatic ionization potential of the order of 2 kcal mol^{-1} and 0.1 eV, respectively. Better agreement with experimental measurements can probably be obtained if these contributions are included in the computations.[88]

All calculations with Gaussian and Turbomole were performed in C_1 symmetry. The minimum character of the resulting stationary points was confirmed by the absence of negative eigenvalues in analytically computed Hessian matrices. In a number of cases, which are documented in Tables 1–6 in the Supporting Information, we observed the occurrence of a single low imaginary mode ($5i$–$70i$ cm^{-1}) in the harmonic frequency analyses. In all cases these imaginary modes correspond to a rotation of one Cp ring out of an almost eclipsed (D_{5h}-like) arrangement. However, geometry optimizations starting from a staggered (D_{5d}-like) arrangement of rings all lead back to the nearly eclipsed conformations. To exclude technical artifacts we checked the influence of the integration grid size (ultrafine) and of the geometry convergence criteria (very tight) settings, but in all cases we were unable to obtain structures without these peculiar imaginary modes. Because these spurious modes spoil the quality of computed zero-point vibrational energies in systematic comparisons, we report here only total energy differences.

For the calibration of computed binding energies (cf. Supporting Information) we performed coupled cluster calculations in combination with the correlation consistent basis set series cc-pVXZ (X = D, T, and Q) of Dunning et al., including an extrapolation to the basis set limit.[89,90] The extrapolation was performed by employing the mixed exponential/Gaussian function $E(x) = E_\infty + b\,e^{-(x-1)} + c\,e^{-(x-1)**2}$, in which x is the cardinal number (DZ = 2, TZ = 3, QZ = 4) and E_∞ the asymptotic value to approximate the basis set limit.[91,92] The underlying molecular structures of the complex and its fragments were optimized at each respective level based on numerically evaluated gradients. These calculations were performed with the program Molpro.[65] As an alternative, computationally much more efficient procedure to extrapolate the CCSD(T) level to the limit of infinite basis-set size, we employed the CBS-QB3 scheme of Peterson et al.[93] as implemented in the Gaussian program. Additional Turbomole calibration calculations were performed with second-order Møller–Plesset perturbation theory in combination with the cc-pVXZ (X = D,T, and Q) series of Dunning. For energies and analytic gradients the RI technique was used in combination with the optimized MP2 auxiliary basis provided in the Turbomole libraries.[94,95]

The AIMPAC program was used for the Bader analysis of the electron density distribution.[96,97] Additional analyses on relevant model complexes were performed with the ADF program package[98–100] at the BP86 level employing an uncontracted Slater-type orbital (STO) basis of polarized triple-ζ quality augmented by two sets of polarization functions.[101] The two 1s core electrons on the carbon and boron atoms and the ten 1s2s2p core electrons on the iron atom were treated by the frozen-core approximation.[102] Scalar relativistic effects were considered by the zero-order regular approximation (ZORA).[103–108] Based on the work of Morokuma[109] and Ziegler and Rauk,[110] the EPA analysis as implemented in the ADF program[111,112,67] partitions the bond dissociation energy D_e for the process A·B → A + B into several contributions. First, D_e is formally separated into the two components ΔE_{INT} and ΔE_{PREP} according to Equation (3)

$$-D_e = \Delta E_{INT} + \Delta E_{PREP} \quad (3)$$

in which ΔE_{INT} is the interaction energy defined as the energy of the complex A·B minus the energies of its constituting fragments A* and B*, which are kept frozen in the geometry and electronic state they adopt in the complex. ΔE_{PREP} then is the energy difference to promote A and B from their equilibrium geometry and electronic state to the geometry and electronic state in A* and B*. ΔE_{INT} can further be divided into three components [Eq. (4)].

$$\Delta E_{INT} = \Delta E_{ELSTAT} + \Delta E_{PAULI} + \Delta E_{ORB} \quad (4)$$

Herein ΔE_{ELSTAT} is the quasiclassical Coulomb interaction energy computed from the frozen electron densities of the fragments A* and B* superimposed at the geometry of the complex. The corresponding electron

density, however, violates the Pauli exclusion principle because it leads to regions of space which are occupied by two electrons of like spin. The Pauli exclusion principle is enforced in the next step by antisymmetrization and renormalization of the Kohn–Sham determinant, which is constructed from the superposition of the formerly noninteracting orbitals of A* and B*. The corresponding change in energy is denoted $\Delta E_{\mathrm{PAULI}}$, the Pauli repulsion term. As last step of the EPA analysis the stabilizing orbital interaction term ΔE_{ORB} is calculated by relaxing the orthonormalized Kohn–Sham orbitals to the optimized Kohn–Sham determinant of the complex. ΔE_{ORB} can be further decomposed into orbital contributions arising from the respective sets of irreducible representations defined by the molecular symmetry. EPA has found widespread application (see, e.g., ref. [113] and refs. 24–26 cited therein). For further details and physical interpretations of the various terms comprising ΔE_{INT}, see the comprehensive exposition by Bickelhaupt and Baerends.[67]

Acknowledgement

M.W. is grateful to the Deutsche Forschungsgemeinschaft (DFG) for financial support. M.C.H. acknowledges support through a Liebig-Habilitation fellowship by the Fonds der Chemischen Industrie. M.S. thanks the Fonds der Chemischen Industrie (FCI) and the Bundesministerium für Bildung und Forschung (BMBF) for a Ph.D. grant. R.H.H. and I.N. are indebted to Assaf Aharoni for meticulously effecting the glove box sample transfers, as noted above. The generous allotment of computer time and excellent service by the CSC Frankfurt, the HHLR Darmstadt, and the HLRS Stuttgart is gratefully acknowledged. The authors wish to thank Prof. Gernot Frenking for stimulating discussions and critical comments on the manuscript.

[1] T. Renk, W. Ruf, W. Siebert, *J. Organomet. Chem.* **1976**, *120*, 1–25.
[2] W. Ruf, T. Renk, W. Siebert, *Z. Naturforsch. B* **1976**, *31*, 1028–1034.
[3] M. Scheibitz, R. F. Winter, M. Bolte, H.-W. Lerner, M. Wagner, *Angew. Chem.* **2003**, *115*, 954–957; *Angew. Chem. Int. Ed.* **2003**, *42*, 924–927.
[4] M. Scheibitz, J. W. Bats, M. Bolte, M. Wagner, *Eur. J. Inorg. Chem.* **2003**, 2049–2053.
[5] M. Fontani, F. Peters, W. Scherer, W. Wachter, M. Wagner, P. Zanello, *Eur. J. Inorg. Chem.* **1998**, 1453–1465.
[6] M. Grosche, E. Herdtweck, F. Peters, M. Wagner, *Organometallics* **1999**, *18*, 4669–4672.
[7] R. E. Dinnebier, M. Wagner, F. Peters, K. Shankland, W. I. F. David, *Z. Anorg. Allg. Chem.* **2000**, *626*, 1400–1405.
[8] W. E. Piers, G. J. Irvine, V. C. Williams, *Eur. J. Inorg. Chem.* **2000**, 2131–2142.
[9] B. E. Carpenter, W. E. Piers, M. Parvez, G. P. A. Yap, S. J. Rettig, *Can. J. Chem.* **2001**, *79*, 857–867.
[10] B. E. Carpenter, W. E. Piers, R. McDonald, *Can. J. Chem.* **2001**, *79*, 291–295.
[11] F. Jäkle, K. Polborn, M. Wagner, *Chem. Ber.* **1996**, *129*, 603–606.
[12] F. Fabrizi de Biani, F. Jäkle, M. Spiegler, M. Wagner, P. Zanello, *Inorg. Chem.* **1997**, *36*, 2103–2111.
[13] E. Herdtweck, F. Peters, W. Scherer, M. Wagner, *Polyhedron* **1998**, *17*, 1149–1157.
[14] S. L. Guo, F. Peters, F. Fabrizi de Biani, J. W. Bats, E. Herdtweck, P. Zanello, M. Wagner, *Inorg. Chem.* **2001**, *40*, 4928–4936.
[15] F. Jäkle, T. Priermeier, M. Wagner, *J. Chem. Soc. Chem. Commun.* **1995**, 1765–1766.
[16] F. Jäkle, T. Priermeier, M. Wagner, *Organometallics* **1996**, *15*, 2033–2040.
[17] E. Herdtweck, F. Jäkle, G. Opromolla, M. Spiegler, M. Wagner, P. Zanello, *Organometallics* **1996**, *15*, 5524–5535.
[18] F. Jäkle, M. Mattner, T. Priermeier, M. Wagner, *J. Organomet. Chem.* **1995**, *502*, 123–130.
[19] M. Herberhold, U. Dörfler, W. Milius, B. Wrackmeyer, *J. Organomet. Chem.* **1995**, *492*, 59–63.
[20] S. Aldridge, C. Bresner, *Coord. Chem. Rev.* **2003**, *244*, 71–92.
[21] K. Ma, M. Scheibitz, S. Scholz, M. Wagner, *J. Organomet. Chem.* **2002**, *652*, 11–19.
[22] A. Appel, F. Jäkle, T. Priermeier, R. Schmid, M. Wagner, *Organometallics* **1996**, *15*, 1188–1194.
[23] M. Scheibitz, J. W. Bats, M. Bolte, H.-W. Lerner, M. Wagner, *Organometallics* **2004**, *23*, 940–942.
[24] B. Wrackmeyer, U. Dörfler, W. Milius, M. Herberhold, *Polyhedron* **1995**, *14*, 1425–1431.
[25] N. Lenze, B. Neumann, A. Salmon, A. Stammler, H.-G. Stammler, P. Jutzi, *J. Organomet. Chem.* **2001**, *619*, 74–87.
[26] A. Appel, H. Nöth, M. Schmidt, *Chem. Ber.* **1995**, *128*, 621–626.
[27] F. Fabrizi de Biani, T. Gmeinwieser, E. Herdtweck, F. Jäkle, F. Laschi, M. Wagner, P. Zanello, *Organometallics* **1997**, *16*, 4776–4787.
[28] F. H. Allen, *Acta Crystallogr. Sect. B* **2002**, *58*, 380–388.
[29] M. J. G. Lesley, A. Woodward, N. J. Taylor, T. B. Marder, I. Cazenobe, I. Ledoux, J. Zyss, A. Thornton, D. W. Bruce, A. K. Kakkar, *Chem. Mater.* **1998**, *10*, 1355–1365.
[30] M. Soriano-Garcia, R. A. Toscano, T. Lopez, A. Campero-Celis, *J. Crystallogr. Spectrosc. Res.* **1987**, *17*, 719–728.
[31] B. Wrackmeyer, U. Dörfler, W. Milius, M. Herberhold, *Z. Naturforsch. B* **1995**, *50*, 201–204.
[32] H. Horn, F. Rudolph, R. Ahlrichs, K. Merzweiler, *Z. Naturforsch. B* **1992**, *47*, 1–4.
[33] J. W. Bats, K. Ma, M. Wagner, *Acta Crystallogr. Sect. C* **2002**, *C58*, m129–m132.
[34] F. Jäkle, A. Berenbaum, A. J. Lough, I. Manners, *Chem. Eur. J.* **2000**, *6*, 2762–2771.
[35] I. Nowik, M. Wagner, R. H. Herber, *J. Organomet. Chem.* **2003**, *688*, 11–14.
[36] R. H. Herber, B. Bildstein, P. Denifl, H. Schottenberger, *Inorg. Chem.* **1997**, *36*, 3586–3592.
[37] H. Schottenberger, K. Wurst, R. H. Herber, *J. Organomet. Chem.* **2001**, *625*, 200–207.
[38] R. H. Herber in *Chemical Mössbauer Spectroscopy* (Ed.: R. H. Herber), Plenum, New York, **1984**, pp. 199–216.
[39] J. Silver, D. A. Davies, R. M. G. Roberts, M. Herberhold, U. Dörfler, B. Wrackmeyer, *J. Organomet. Chem.* **1999**, *590*, 71–76.
[40] A. Houlton, J. R. Miller, R. M. G. Roberts, J. Silver, *J. Chem. Soc. Dalton Trans.* **1990**, 2181–2184.
[41] J. Pebler, W. Ruf, W. Siebert, *Z. Anorg. Allg. Chem.* **1976**, *422*, 39–42.
[42] V. I. Gol'danskii, E. F. Makarov in *Chemical Applications of Mössbauer Spectroscopy* (Eds.: V. I. Gol′danskii, R. H. Herber), Academic Press, New York, **1968**, pp. 102–107.
[43] I. Nowik, R. H. Herber, *J. Phys. Chem. Solids* **2003**, *64*, 313–317; 1225.
[44] T. C. Gibb in *Principles of Mössbauer Spectoscopy*, Chapman and Hall, London, **1976**, pp. 97–100.
[45] A. E. Reed, F. Weinhold, *J. Chem. Phys.* **1983**, *78*, 4066–4073.
[46] A. E. Reed, R. B. Weinstock, F. Weinhold, *J. Chem. Phys.* **1985**, *83*, 735–746.
[47] A. Appel, F. Jäkle, T. Priermeier, R. Schmid, M. Wagner, *Organometallics* **1996**, *15*, 1188–1194.
[48] K. B. Wiberg, *Tetrahedron* **1968**, *24*, 1083–1096.
[49] C. E. Moore, *Atomic Energy Levels*, *Vol. 467*, U.S. National Bureau of Standards, **1949**.
[50] R. H. Blessing, *Acta Crystallogr. Sect. A* **1995**, *51*, 33–38.
[51] A. L. Spek, *Acta Crystallogr. Sect. A* **1990**, *46*, C34.
[52] G. M. Sheldrick, Siemens Analytical X-ray Instruments Inc., Madison, Wisconsin (USA), **1996**.
[53] G. M. Sheldrick, *Acta Crystallogr. Sect. A* **1990**, *46*, 467–473.
[54] SHELXL-97, A program for the refinement of crystal structures, G. M. Sheldrick, Universität Göttingen, **1997**.
[55] R. F. Winter, F. M. Hornung, *Organometallics* **1999**, *18*, 4005–4014.
[56] R. H. Herber, I. Nowik, *Hyperfine Interact.* **2001**, *136*, 699–703.

[57] I. Nowik, R. H. Herber, *Inorg. Chim. Acta* **2000**, *310*, 191–195.
[58] R. H. Herber, I. Nowik, *Hyperfine Interact.* **2000**, *126*, 127–130.
[59] Gaussian 03, Revision B.3, M. J. Frisch, G. W. Trucks, H. B. Schlegel, G. E. Scuseria, M. A. Robb, J. R. Cheeseman, J. J. A. Montgomery, T. Vreven, K. N. Kudin, J. C. Burant, J. M. Millam, S. S. Iyengar, J. Tomasi, V. Barone, B. Mennucci, M. Cossi, G. Scalmani, N. Rega, G. A. Petersson, H. Nakatsuji, M. Hada, M. Ehara, K. Toyota, R. Fukuda, J. Hasegawa, M. Ishida, T. Nakajima, Y. Honda, O. Kitao, H. Nakai, M. Klene, X. Li, J. E. Knox, H. P. Hratchian, J. B. Cross, C. Adamo, J. Jaramillo, R. Gomperts, R. E. Stratmann, O. Yazyev, A. J. Austin, R. Cammi, C. Pomelli, J. W. Ochterski, P. Y. Ayala, K. Morokuma, G. A. Voth, P. Salvador, J. J. Dannenberg, V. G. Zakrzewski, S. Dapprich, A. D. Daniels, M. C. Strain, O. Farkas, D. K. Malick, A. D. Rabuck, K. Raghavachari, J. B. Foresman, J. V. Ortiz, Q. Cui, A. G. Baboul, S. Clifford, J. Cioslowski, B. B. Stefanov, G. Liu, A. Liashenko, P. Piskorz, I. Komaromi, R. L. Martin, D. J. Fox, T. Keith, M. A. Al-Laham, C. Y. Peng, A. Nanayakkara, M. Challacombe, P. M. W. Gill, B. Johnson, W. Chen, M. W. Wong, C. Gonzalez, J. A. Pople, Gaussian, Inc, Pittsburgh, PA, **2003**.
[60] Turbomole—program system for ab initio electronic structure calculations, Version 5.6., R. Ahlrichs, M. Bär, H. P. Baron, R. Bauernschmitt, S. Böcker, M. Ehrig, K. Eichkorn, S. Elliott, F. Furche, F. Haase, M. Häser, C. Hättig, H. Horn, C. Huber, U. Huniar, M. Kattanek, A. Köhn, C. Kölmel, M. Kollwitz, K. May, C. Ochsenfeld, H. Öhm, A. Schäfer, U. Schneider, O. Treutler, K. Tsereteli, B. Unterreiner, M. von Arnim, F. Weigend, P. Weis, H. Weiss, Universität Karlsruhe, Germany, **2002**.
[61] R. Ahlrichs in *Encyclopedia Computational Chemistry* (Ed.: P. von R. Schleyer), Wiley, Chichester, **1998**, pp. 3123–3129.
[62] M. von Arnim, R. Ahlrichs, *J. Comput. Chem.* **1998**, *19*, 1746–1757.
[63] O. Treutler, R. Ahlrichs, *J. Chem. Phys.* **1995**, *102*, 346–354.
[64] R. Ahlrichs, M. Bär, M. Häser, H. Horn, C. Kölmel, *Chem. Phys. Lett.* **1989**, *162*, 165–169.
[65] MOLPRO, Version 2002.6, R. D. Amos, A. Bernhardsson, A. Berning, P. Celani, D. L. Cooper, M. J. O. Deegan, A. J. Dobbyn, F. Eckert, C. Hampel, G. Hetzer, P. J. Knowles, T. Korona, R. Lindh, A. W. Lloyd, S. J. McNicholas, F. R. Manby, W. Meyer, M. E. Mura, A. Nicklass, P. Palmieri, R. Pitzer, G. Rauhut, M. Schütz, U. Schumann, H. Stoll, A. J. Stone, R. Tarroni, T. Thorsteinsson, H.-J. Werner.
[66] G. te Velde, F. M. Bickelhaupt, E. J. Baerends, S. J. A. van Gisbergen, C. Fonseca Guerra, J. G. Snijders, T. Ziegler, *J. Comput. Chem.* **2001**, *22*, 931.
[67] F. M. Bickelhaupt, E. J. Baerends in *Reviews in Computational Chemistry*, *Vol. 15* (Eds.: K. B. Lipkowitz, D. B. Boyd), Wiley-VCH, New York, **2000**, pp. 1–86.
[68] A. D. Becke, *Phys. Rev. A* **1988**, *38*, 3098–3100.
[69] J. B. Perdew, *Phys. Rev. B* **1986**, *33*, 8822–8824.
[70] F. A. Hamprecht, A. J. Cohen, D. J. Tozer, N. C. Handy, *J. Chem. Phys.* **1998**, *109*, 6264–6271.
[71] A. D. Boese, N. L. Doltsinis, N. C. Handy, M. Sprik, *J. Chem. Phys.* **2000**, *112*, 1670–1678.
[72] A. D. Boese, N. C. Handy, *J. Chem. Phys.* **2001**, *114*, 5497–5503.
[73] K. Eichkorn, O. Treutler, H. Öhm, M. Häser, R. Ahlrichs, *Chem. Phys. Lett.* **1995**, *240*, 283–289.
[74] R. A. Kendall, H. A. Früchtl, *Theor. Chem. Acc.* **1997**, *97*, 158–163.
[75] B. I. Dunlap, *J. Mol. Struct. (THEOCHEM)* **2000**, *529*, 37.
[76] B. I. Dunlap, *J. Chem. Phys.* **1983**, *78*, 3140–3142.
[77] K. Eichkorn, F. Weigend, O. Treutler, R. Ahlrichs, *Theor. Chim. Acta* **1997**, *97*, 119–124.
[78] A. D. Becke, *J. Chem. Phys.* **1993**, *98*, 5648–5652.
[79] P. J. Stephens, F. J. Devlin, C. F. Chabalowski, M. J. Frisch, *J. Phys. Chem.* **1994**, *98*, 11623–11627.
[80] A. D. Becke, *J. Chem. Phys.* **1997**, *107*, 8554–8560.
[81] H. L. Schmider, A. D. Becke, *J. Chem. Phys.* **1998**, *108*, 9624–9631.
[82] A. Schäfer, H. Horn, R. Ahlrichs, *J. Chem. Phys.* **1992**, *97*, 2571–2577.
[83] A. Schäfer, C. Huber, R. Ahlrichs, *J. Chem. Phys.* **1994**, *100*, 5829–5835.
[84] N. Godbout, D. R. Salahub, J. Andzelm, E. Wimmer, *Can. J. Chem.* **1992**, *70*, 560–571.
[85] A. Klamt, G. Schüürmann, *J. Chem. Soc. Perkin Trans. 1* **1993**, *2*, 799–805.
[86] P. Schwerdtfeger, M. Dolg, W. H. E. Schwarz, G. A. Bowmaker, P. D. W. Boyd, *J. Chem. Phys.* **1989**, *91*, 1762–1774.
[87] A. Bergner, M. Dolg, W. Kuechle, H. Stoll, H. Preuss, *Mol. Phys.* **1993**, *80*, 1431–1441.
[88] P. Winget, E. J. Weber, C. J. Cramer, D. G. Truhlar, *Phys. Chem. Chem. Phys.* **2000**, *2*, 1231–1239.
[89] T. H. Dunning, Jr., *J. Chem. Phys* **1989**, *90*, 1007–1023.
[90] T. H. Dunning, Jr., *J. Phys. Chem. A* **2000**, *104*, 9062–9080.
[91] K. A. Peterson, D. E. Woon, T. H. Dunning, Jr., *J. Chem. Phys* **1994**, *100*, 7410–7415.
[92] D. E. Woon, T. H. Dunning, Jr., *J. Chem. Phys* **1994**, *101*, 8877–8893.
[93] J. J. A. Montgomery, M. J. Frisch, J. W. Ochterski, G. A. Petersson, *J. Chem. Phys.* **1999**, *110*, 2822–2827.
[94] F. Weigend, M. Häser, *Theor. Chem. Acc.* **1997**, *97*, 331–340.
[95] F. Weigend, M. Häser, H. Patzelt, R. Ahlrichs, *Chem. Phys. Lett.* **1998**, *294*, 143–152.
[96] AIMPAC95 program package, R. F. W. Bader, McMaster University, Hamilton, ON, Canada, **1995**.
[97] F. W. Biegler-König, R. F. W. Bader, *J. Comput. Chem.* **1982**, *3*, 317–328.
[98] ADF2003.1, SCM, Theoretical Chemistry, Vrije Universiteit, Amsterdam, **2003**, http://www.scm.com.
[99] C. Fonseca Guerra, J. G. Snijders, G. te Velde, E. J. Baerends, *Theor. Chem. Acc.* **1998**, *99*, 391–403.
[100] G. te Velde, F. M. Bickelhaupt, E. J. Baerends, S. J. A. van Gisbergen, C. Fonseca Guerra, J. G. Snijders, T. Ziegler, *J. Comput. Chem.* **2001**, *22*, 931–967.
[101] J. G. Snijders, E. J. Baerends, P. Vernooijs, *At. Data Nucl. Data Tables* **1982**, *26*, 483.
[102] E. J. Baerends, D. E. Ellis, P. Ros, *Chem. Phys.* **1973**, *2*, 41–51.
[103] E. van Lenthe, E. J. Baerends, J. G. Snijders, *J. Chem. Phys.* **1993**, *99*, 4597–4610.
[104] E. van Lenthe, E. J. Baerends, J. G. Snijders, *J. Chem. Phys.* **1994**, *101*, 9783–9792.
[105] E. van Lenthe, A. E. Ehlers, E. J. Baerends, *J. Chem. Phys.* **1999**, *110*, 8943–8953.
[106] C. Chang, M. Pelissier, P. Durand, *Phys. Scr.* **1986**, *34*, 394–404.
[107] J.-L. Heully, I. Lindgren, E. Lindroth, S. Lundquist, A.-M. Martensson-Pendrill, *J. Phys. B* **1986**, *18*, 2799–2815.
[108] J. G. Snijders, A. H. Sadlej, *Chem. Phys. Lett.* **1996**, *252*, 51–61.
[109] K. Morokuma, *J. Chem. Phys.* **1971**, *55*, 1236–1244.
[110] T. Ziegler, A. Rauk, *Theor. Chim. Acta* **1977**, *46*, 1–10.
[111] T. Ziegler, A. Rauk, *Inorg. Chem.* **1979**, *18*, 1558–1565.
[112] T. Ziegler, A. Rauk, *Inorg. Chem.* **1979**, *18*, 1755–1759.
[113] F. Bessac, G. Frenking, *Inorg. Chem.* **2003**, *42*, 7990–7994.
[114] G. Schaftenaar, J. H. Noordik, *J. Comput.-Aided Mol. Des.* **2000**, *14*, 123–134.
[115] Z.-F. Xu, Y. Xie, W.-L. Feng, H. F. Schaefer III, *J. Phys. Chem. A* **2003**, *107*, 2716–2729.

Received: July 7, 2004
Published online: December 3, 2004

